Mapping Geohazards in the Churia Region of Nepal: An Application of Remote Sensing and Geographic Information Systems

A Thesis

Presented to the

Graduate Faculty of the

University of Louisiana at Lafayette

In Partial Fulfillment of the

Requirements for the Degree

Master of Science

Terri Bannister

Fall 2016

Mapping Geohazards in the Churia Region of Nepal: An Application of Remote Sensing and
Geographic Information Systems

Terri Bannister

APPROVED:

_____   _____
Durga D. Poudel, Chair   Carl Richter
Professor of Environmental Science   Professor of Geology

_____   _____
Timothy W. Duex   Mary Farmer-Kaiser
Associate Professor of Geology   Dean of the Graduate School

ABSTRACT

The Churia region of Nepal is experiencing serious environmental degradation due to

landslides, monsoon flooding, land use changes, and gravel excavation. The objectives of this

study were to quantify the temporal change of landslides as related to changes in land

use/deforestation/urbanization, to quantify the temporal change and extent of river inundation

in the Terai, to quantify the extent to which stone quarrying exacerbates the degradation

process, and to generate a landslide hazard risk map. Gravel extraction and precipitation data,

along with field work and geospatial methods, were used to map degradation by focusing on

the centrally located districts of Bara, Rautahat, and Makwanpur. Landsat land use

classifications were conducted on imagery from 1976, 1988, 1999, and 2015. A modified

Normalized Difference Mid-Infrared (NDMIDIR) algorithm was created by incorporating

slope, elevation, and land use types to identify landslide scars. A GIS model using weighted

landslide variables derived from remote sensing and GIS methods to predict landslide

susceptibility was created. These variables include hydrology, settlement, lithology, geology,

precipitation, infrastructure, elevation, slope, aspect, land use, and previous landslides.

Gravel excavation in 2007/2008 was nearly 700% higher than in 2001/2002. The Normalized

Difference Vegetation Index (NDVI) results showed that the study area is losing 1.03%

forest cover annually; in 1977, there was 70% forest cover, but only 32% forest cover

remained in 2016. The accuracy assessment of the 2015 Landsat 8 land use classification was

79%. NDMIDIR results showed that from 1988 to 2016, the total area representing landslide scars increased from 7.26km^2 to 8.73 km^2. The weighted variable GIS model output map indicated that 70% of the Siwalik zone and southern Lesser Himalayan zone in the three study districts have significant risk of landslides. Landslides and flooding from heavy monsoon rain, deforestation to develop agriculture and urbanization, and gravel extraction have caused rapid and ongoing environmental degradation in the Churia region of Nepal. Results provide information for disaster management and assist policy planners in landslide prone areas decrease loss of lives and property.

ACKNOWLEDGMENTS

TABLE OF CONTENTS

LIST OF FIGURES

LIST OF TABLES

LIST OF EQUATIONS

LIST OF ABBREVIATIONS

μm	micrometer
cm	centimeter
km	kilometer
m	meter
mm	millimeter
ALOS	Advanced Land Observing Satellite
AOI	Area of Interest
DEM	Digital Elevation Model
ETM+	Landsat Enhanced 7 Thematic Mapper Plus
FBS	Fine Beam Single Polarization
GIS	Geographic Information Systems
InSAR	Interferometric Synthetic Aperture Radar
ISOCLUS	Iterative self-organizing Clustering
IWS	Sentinel 1A Interferometric Wide Swath mode
JERS-1	Japanese Earth Resources Satellite-1
masl	Meters Above Sea Level
MBT	Main Boundary Thrust
MCT	Main Central Thrust
MFT	Main Frontal Thrust
MSS	Landsat Multi Spectral Scanner
NASA	National Aeronautics and Space Administration
NDMIDIR	Normalized Difference Mid-Infrared

NDVI   Normalized Difference Vegetation Index

NIR   Near-infrared

OLI   Landsat 8 Operational Land Imager

PALSAR   Phased Array type L-band Synthetic Aperture Radar

RADAR   Radio Detection and Ranging

SAR   Synthetic Aperture Radar

SNAP   Sentinels Application Platform

SWIR   Short-wave Infrared

TM   Landsat 5 Thematic Mapper

USD   US dollars

USGS   United States Geological Survey

UTM   Universal Transverse Mercator

WGS84   World Geodetic System 1984

CHAPTER ONE: INTRODUCTION

1.1   THE STUDY AREA

Nepal has five major geological zones: Terai, Siwalik, Lesser Himalayan, Higher Himalayan, and the Tibetan Tethys (Figure 1). The Churia region consists of both the Terai and Siwalik zones. Bara and Rautahat were selected for this study as they are centrally located in the Nepal and span the Terai and Siwalik zones. Makwanpur was added to the study because a landslide dataset was located to use for algorithm validation purposes. The Siwalik hills rise steeply from the Terai plains and represent the first and lowest hogback ridges of the Himalayas that span the entire west to east length of Nepal (Rastrapati Chure Conservation Program, date unknown). While the Terai is flat and ideal for agriculture, the steep and fragile slopes of the Siwalik are composed of weak, unconsolidated, sedimentary materials prone to landslides (Kandel, 2009; Pokhrel, 2013; Rastrapati Chure Conservation Program, date unknown).
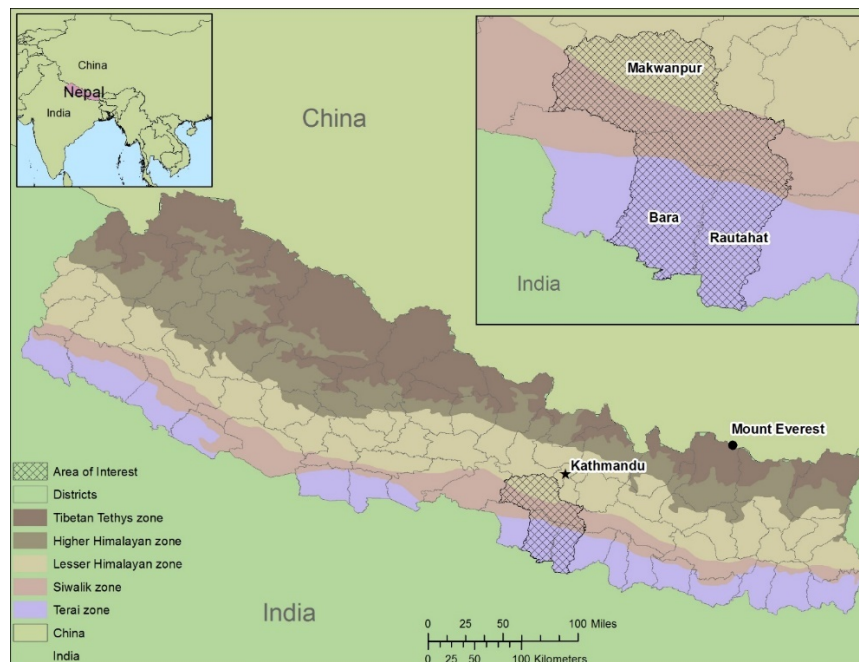
Figure 1. Study area and Nepal physiographic zones. The top left inset map shows the location of Nepal in relation to India, China, and much of Asia. The top right inset shows the three districts that comprise the study area.

Monsoon season dominates Nepal's annual rainfall. From June to September, this rainy season is marked by humid south-westerly winds from India that rise as they meet the hills and mountains of Nepal, generating 80% of Nepal's annual precipitation (Brewin et al., 2000; Panthi et al., 2015). Topography influences rainfall distribution; while rainfall increases with altitude from the Terai to the Siwalik, moving north from the Lesser Himalayan and the Higher Himalayan zone, the area experiences a decrease in rainfall above 2800 masl (Brewin et al., 2000). Figure 2 shows that the Churia region, especially the Siwalik hills, is most vulnerable to rainfall induced landslides and flooding during monsoon season (Panthi et al., 2015). The graph shows that minimum rainfall occurs during the winter post-monsoon season (October to March). The pre-monsoon season (April to June) is considered a transition between winter and the monsoon, which can experience light rainfall from local storms (Brewin et al., 2000; Panthi et al., 2015). In recent years, rainfall data shows that precipitation intensity and magnitude are increased in the monsoon and post-monsoon seasons, which increase the potential for flooding and landslide events (Devkota, 2014). The trend is justified by the perceptions of the local populations that suffer the consequences of these events including damage to crops, physical and social infrastructure, environment, lives and livelihood and weakening the capacity of rural poor (Devkota, 2014).
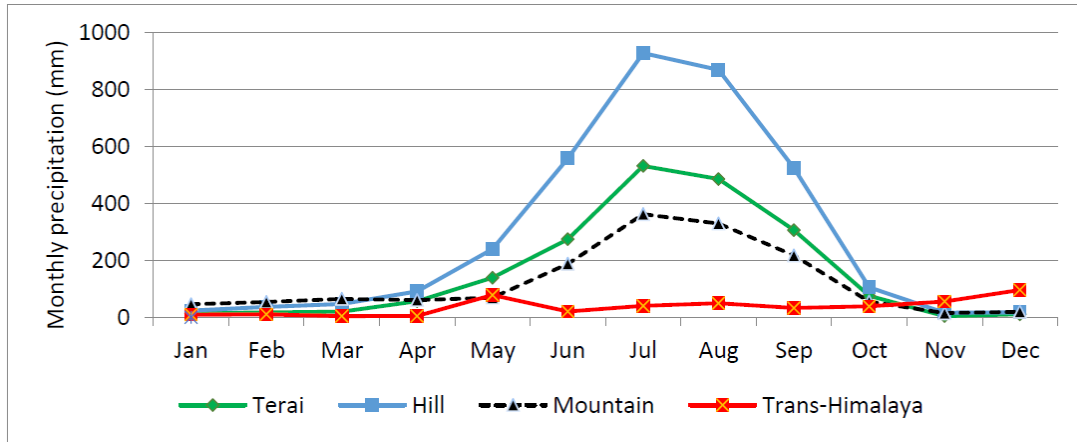
Figure 2. Monthly average precipitation in the different zones of Nepal. From Panthi et al. (2015).

Landslides are common in Nepal, especially the Siwalik Hill zone, during monsoon season when lives, property, livelihoods, environment, and infrastructure are no match to the force of these landslides (Dahal et al., 2009). Nepal represents 30% of landslides globally, and the nation annually experiences economic loss because of landslide damage valued at more than $1 billion USD (Dahal et al., 2009).

In the Terai, 80% of the population are farmers and use indigenous agricultural production practices (Devkota, 2014). This is representative of the entire Churia region, which is dependent on subsistence farming to survive (Kandel, 2009; Pokhrel, 2013). Climate related natural hazards such as floods and droughts affect subsistence agriculture, people's livelihood, and weaken the national economy (Devkota, 2014). Immense and haphazard settlement has taken place for more than forty years as the threat of malaria became less severe (Pokhrel, 2013). The Terai represents about 20% of the area of Nepal, yet nearly 50% of Nepal's population live on the plains, and this unsustainable demand on the Terai grows daily as migration from the mountains, Siwalik, urban areas, and international

locations persists (Sudmeier et al., 2013). In the Churia, more than 80% of these households do not have ownership of the land on which they live and work (Pokhrel, 2013). Approximately 7% of Nepal's population of over 26.5 million live in the study area (Government of Nepal National Planning Commission Secretariat, 2012). The study area covers 3% of the total area of Nepal and approximately 12% of the Churia region. While the nation was once extensively covered by forest, the Churia region has been and continues to be depleted in both quantity and quality of forest cover as at least 75% of households rely on hardwood timber from the Terai for fuel (Kandel, 2009). Besides needing the timber for fuel, forests are cleared for agriculture, livestock grazing, and infrastructure development (Tembe, 2001, Kandel, 2009; Pokhrel, 2013).

Illegal excavation of gravels from rivers in the Churia region has been rampant and fueled by the construction industry in India as well as within Nepal (Raut and Panthi, 2015). Locals and conservationists in Nepal report that the problem stems from the failure of the government to implement and manage programs to issue leases for, and thereby regulate, the extraction of the river materials (Pokhrel, 2013; Raut and Panthi, 2015). As boulders and other river materials are excavated, the river velocities increase, damaging infrastructure, threatening the lives of humans and cattle, and washing away homes and farmland (Raut and Panthi, 2015).

1.2   HIMALAYAS

The Himalayan orogeny is a textbook example of mountain building resulting from continent-on-continent collision of the Indian and Eurasian plates, combining rapid shortening and thickening of the crust (Upreti, 1999; Gokarn et al., 2002, Yin, 2006; Shanker et al., 2011). This highly deformed upper crust spans 2500 km and is dominated by thrust and

4

normal and transverse faults (Upreti, 1999; Shanker et al., 2011). Figure 3 illustrates how the main tectonic features that control the tectonic framework of the Himalayas, and which are nearly parallel to each other, developed from oldest in the north to youngest in the south, are the Main Central Thrust (MCT), Main Boundary Thurst (MBT), and Main Frontal Thurst (MFT) (Upreti, 1999; Shanker et al., 2011).
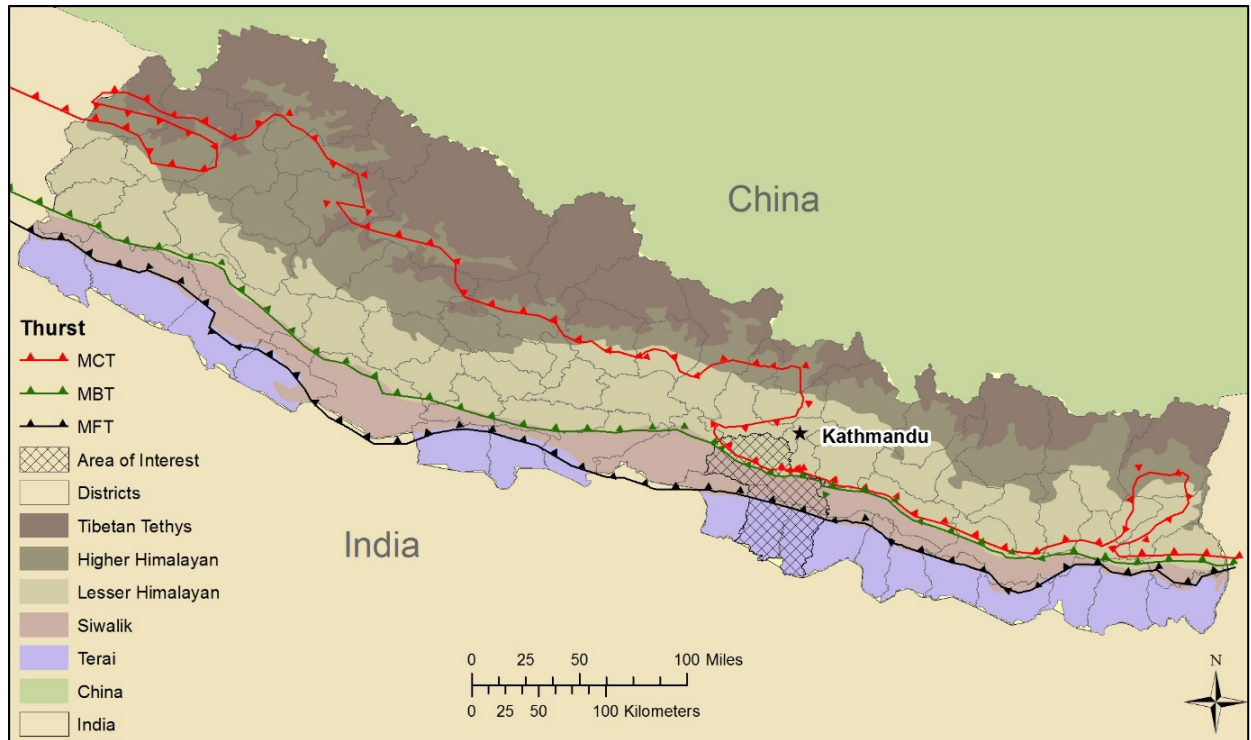
Figure 3. Study area and main thrust belts of the Himalayas.

1.3   REMOTE SENSING SENSORS AND APPLICATIONS

Synthetic Aperture Radar (SAR) can operate in darkness and penetrate cloud cover, which is often paramount during rainy conditions such as monsoons (Lillesand et al., 2015). Additionally, SAR has longer wavelengths than optical data, allowing SAR to penetrate vegetation which might be overshadowing flood inundation (Lillesand et al., 2015). Table 1 identifies the SAR sensors used for this study and the characteristics for each sensor.

Table 1. Sensor characteristics of the SAR data used. Summarized from European Space Agency (2016a).

Mission	Operational	Revisit (days)	Polarizations	Spectral Bands	Wavelength	Resolution (m)	Scene size (km)
RSAT-1 SAR ST4	1995-present	24	HH	C	5.6 cm	30	100
JERS-1 SAR	1992 - 1998	44	HH	L	23.5 cm	18	75
PALSAR (FBS)	2006-2011	46	HH or VV	L	23.62 cm	10	70
Sentinel 1A IWS	2014-present	12	HH+HV, VH+VV, HH, VV	C	5.6 cm	5 x 20	250

The Landsat program began in the early 1970s and has been used globally for a wide range of research, including agriculture, geology, forestry, and surveillance (Lillesand et al., 2015). Unlike SAR sensors, Landsat requires the sun's illumination to collect imagery and is unable to penetrate cloud cover (Lillesand et al., 2015). Landsat operates in the visible, infrared, and thermal wavelengths. Table 2 identifies the characteristic of the Landsat sensors used for this study.

Table 2. Sensor characteristics of the Optical (Landsat) data used. Summarized from NASA (2016).

Mission	Operational	Revisit period (days)	Spectral Bands	Wavelength (µm)	Resolution (m)	Scene size (km)
Landsat 2 MSS	1975-1982	18	Band 4 - green	0.5 - 0.6	60	170 x 185
			Band 5 – red	0.6 - 0.7		
			Band 6 - NIR	0.7 - 0.8		
			Band 7 - NIR	0.8 - 1.1		
Landsat 5 TM; Landsat 7 ETM+	1984-2013; 1999-present	16	Band 1 - blue	0.45 - 0.52	30	170 x 183
			Band 2 - green	0.52 - 0.60		
			Band 3 – red	0.63 - 0.69		
			Band 4 - NIR	0.77 - 0.90		
			Band 5 – SWIR 1	1.55 - 1.75		
			Band 6 - Thermal Infrared	10.40 - 12.50	120	
			Band 7 – SWIR 2	2.09 - 2.35	30	
			Band 8 - Panchromatic (Landsat 7 only)	0.52 - 0.90	15	
Landsat 8 OLI	2013-present	16	Band 1 – coastal aerosol	0.43 - 0.45	30	
			Band 2 – blue	0.45 - 0.51		
			Band 3 - green	0.53 - 0.59		
			Band 4 – red	0.64 - 0.67		
			Band 5 - NIR	0.85-0.88		
			Band 6 - SWIR 1	1.57 - 1.65		
			Band 7 SWIR 2	2.11 - 2.29		
			Band 8 - Panchromatic	0.50 - 0.68	15	
			Band 9 – Cirrus	1.36 - 1.38	30	
			Band 10 – Thermal Infrared 1	10.60 – 11.19	100	
			Band 11 – Thermal Infrared 2	11.5 - 12.51		

In terms of remote sensing, there are two types of classifications: supervised and unsupervised. Both make use of the spectral information of the pixels of the raster bands of the imagery. However, the unsupervised option is more computer-automated, as the user simply specifies how many classes to output, which bands of the image to consider for the calculation, and how large a window to do each calculation (PCI Geomatica, 2016). The unsupervised classification algorithm then organizes the image information into discrete classes of spectrally similar pixel values, which the operator then assigns to the desired classes (PCI Geomatica, 2016). There are several types of unsupervised classifications, including K-means, Fuzzy K-means, and ISOCLUS (PCI Geomatica, 2016). The ISOCLUS algorithm runs an iterative process to group the pixels spectrally by calculating the mean of the cluster to the value of each pixel, based on the user defined number repetitions and the minimum Euclidean distance when assigning each pixel to a cluster (PCI Geomatica, 2016). After running the user defined number of iterations, the migration of cells from one cluster to another is minimal, and the clusters are considered stable (PCI Geomatica, 2016).

An accuracy assessment measures the agreement by comparing geographically correct and known land use points to the classification output image of unknown quality; typically the accuracy assessment includes a matrix comparing the known land use points and the classification outputs (Lillesand et al., 2015). A classification is only as good as the level of confidence reported by the accuracy assessment (Lillesand et al., 2015).

1.4   OBJECTIVES

The objectives of this study are to (1) quantify the temporal change of landslides in the Churia region and correlate with temporal changes in land use/deforestation/urbanization in the region, (2) quantify the temporal change of river inundation in Terai, especially during

monsoon seasons, and quantify the extent inundation exacerbates the Churia degradation

process, (3) quantify the extent stone quarrying exacerbates the Churia degradation process,

and (4) generate a landslide hazard risk map. As part of this project, the hypothesis will be

tested that the Churia region is being degraded as a result of landslides, flooding, land use

change, and gravel excavation. The expectation is that the Churia region is being degraded as

a result of these factors at an increasingly alarming rate. In the future, the data related to the

results of these objectives will be provided to those responsible for designing policy in Nepal

for consideration as they plan for conservation and resource management of the Churia

region.

CHAPTER TWO: LITERATURE REVIEW

2.1   REGIONAL GEOLOGY

The Himalayan range extends 2500 km from Pakistan to the far northeastern reaches of India and formed as a result of the Indian and Eurasian plates colliding, which in an ongoing process (Upreti, 1999; Yin, 2006; Shanker et al., 2011). Geologically and geographically, Nepal can be divided into five zones that run laterally from east to west: the Terai, Siwalik, Lesser Himalayan, Higher Himalayan, and Tibetan Tethys. Table 3 summarizes the characteristics of the zones.

Table 3. Geological zones of Nepal. Modified after Upreti (1999) and Hasegawa et al. (2009a).

Geological Zone	Altitude (masl)	Main Rock Types	Geomorphological processes	Age
Terai	100-200	Alluvium; course in north, finer southward. Foreland basin deposits	Deposition and erosion by rivers and tectonic uplift	Pleistocene to present
Siwalik	200-1000	sandstone, mudstone, shale, and conglomerate. Mollase deposits of the Himalaya	Tectonic uplift, erosion, landslides	Mid-Miocene to Pleistocene
Lesser Himalayan Zone	1000-5000	Schist, phyllite, gneiss, quartzite, granite and limestone		Precambrian and Paleozoic; Mesozoic
Higher Himalayan Zone	> 5000	Gneisses, schists, and marble	Tectonic uplift, weathering, erosion (rivers, wind, and glaciers), and landslides	Precambrian
Tibetan Tethys Zone	2500-4000	Gneisses schists and marble. Also, limestones, shale, sandstones		

The Terai extends from the border with India to the base of Siwalik hills (Nakayama and Ulak, 1999; Syangbo and Tamrakar, 2013; Tamrakar and Syangbo, 2014). Geologically, this zone is composed of alluvium deposits consisting of coarser sediments in the north and

finer sediment, like silt, in the southern part (Nakayama and Ulak, 1999; Syangbo and Tamrakar, 2013; Tamrakar and Syangbo, 2014).

The Siwalik zone represents the lower hills of the Churia region that lies between the MFT in the south and MBT in the north (Nakayama and Ulak, 1999; Syangbo and Tamrakar, 2013; Tamrakar and Syangbo, 2014). The Siwalik dates to Middle Miocene to Early Pleistocene (Nakayama and Ulak, 1999; Syangbo and Tamrakar, 2013; Tamrakar and Syangbo, 2014). The zone is comprised of loose to consolidated north dipping sedimentary rocks such as conglomerates, silt stone, mudstone, and marls (Nakayama and Ulak, 1999; Syangbo and Tamrakar, 2013; Tamrakar and Syangbo, 2014). Based on lithology, the Siwalik zone can be further divided into three regions: Upper Siwalik, Middle Siwalik, and Lower Siwalik, which consist of conglomerates, sandstone, and fine sandstone/mudstone, respectively (Nakayama and Ulak, 1999; Syangbo and Tamrakar, 2013; Tamrakar and Syangbo, 2014).

The three northern most geological and geographic zones are the Lesser Himalayan, Higher Himalaya, and Tibetan Tethys. The Lesser Himalayan zone is separated from the Siwaliks by the MBT. The Lesser Himalaya is comprised of metamorphic rock like slate, phyllite, schist, quartzite, marble, and sedimentary rocks such as limestone and dolomite and shale in the south (Upreti, 1999; Yin, 2006). Further north, the Higher Himalayan zone is separated from the Lesser Himalaya zone by the MCT. The Higher Himalayas are comprised of metamorphic rocks such as gneisses, schist quartzite, and marbles (Upreti, 1999; Yin, 2006). This zone has high snowpack, steep topography, extremely high relief, rocky cliff, and outcrops with very little top soil (Upreti, 1999; Yin, 2006). Conversely, the Tibetan Tethys zone, which is the northern zone in Nepal, is a wide, rugged, and rocky valley with low

11
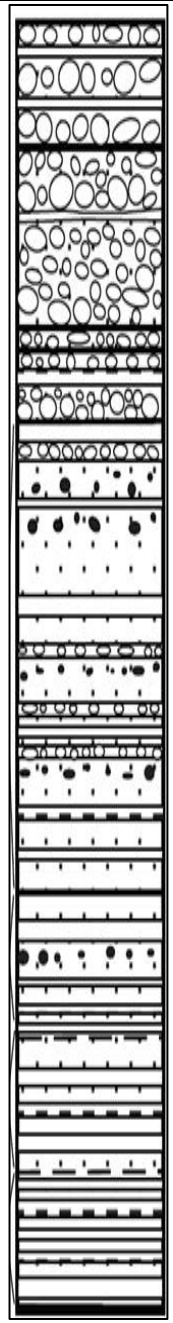
relief, covered by thick glacial and fluvial-glacial deposits of fossiliferous sedimentary rocks such as shale, limestone, and sandstone, with some very loose and fragile recent alluvium (Upreti, 1999; Yin, 2006; Shanker et al., 2011).

The three tectonic thrust belts in Nepal, from south to north, are the Main Frontal Thrust (MFT), Main Boundary Thrust (MBT), and Main Central Thrust (MCT). These belts are extremely hazardous and tremendous triggers for landslides and other forms of mass movement (Nakayama and Ulak, 1999; Upreti, 1999; Yin, 2006; Shanker et al., 2011; Syangbo and Tamrakar, 2013; Tamrakar and Syangbo, 2014). The MFT, located at the boundary between Terai and Siwalik, is the youngest of the three fault belts and is considered active (Nakayama and Ulak, 1999; Syangbo and Tamrakar, 2013; Tamrakar and Syangbo, 2014). The MBT also considered to be active tectonically, is older than the MFT, and represents the contact between the Lesser Himalayan zone and the Siwalik zone (Nakayama and Ulak, 1999; Syangbo and Tamrakar, 2013; Tamrakar and Syangbo, 2014). The MBT has been the source of very large earthquakes (Upreti, 1999; Yin, 2006; Shanker et al., 2011). The MCT is a north dipping thrust fault representing the tectonic contact between the Higher Himalayan zone and Lesser Himalayan zone and at one time was a convergent plate boundary (Upreti, 1999; Yin, 2006; Shanker et al., 2011). While active during the early stages of Himalayan orogeny, the MCT is less active than the other two thrust belts (Upreti, 1999; Yin, 2006; Shanker et al., 2011).

2.2   CHURIA REGION GEOLOGY

The four main geological units of the overall Churia region, from oldest to youngest, are the Rapti Formation, Amlekhganj Formation, Churia Khola Formation, and the Churia Mai Formation; the Amlekhganj and Rapti are each further divided into the upper, middle,

12

and lower members (Nakayama and Ulak, 1999; Sigdel et al., 2011; Tamrakar and Khakurel,

2012). Figure 4 summarize these formations, stratigraphy, and depositional environments.

	Formation	Member	Thickness (m)	Interpretation	Lithology
	Churia Mai		500+	Debris flow	Poorly sorted boulder conglomerates, mudstone; lower part sandstone
	Churia Khola		1100	Gravelly braided system	Poorly sorted, loosely consolidated cobble-pebble conglomerate
	Amlekhganj	Upper	2100	Sandy braided system	Cross-bedded, very coarse grained, pebbly "salt and pepper" sandstones, mudstone
		Middle	600		
		Lower	340	Flood flow dominated meandering stream system	
	Rapti	Upper	450		
		Middle	350	Meandering stream	Cross-laminated to massive and fine-to medium-grained sandstone, siltstone and mudstone
		Lower	210+		Cross-laminated and fine- to medium-grained sandstones, mudstone, siltstone, and mudstone

Figure 4. Stratigraphy of the Churia region. Compiled from Nakayama and Ulak (1999),
Sigdel et al. (2011), and Tamrakar and Khakurel (2012).

Nakayama and Ulak (1999) examined the facies of the Churia region south of Hetauda, Makwanpur and summarized the Rapti Formation as consisting of very fine- to medium-grained gray sandstones and mudstones. More specifically, the Lower Middle Rapti Formation was interpreted as a meandering system where the Lower member has more mudstone than sandstone, while the Middle member has equal proportions of sandstones and mudstones, and the Upper member is primarily composed of fine- to coarse-grained sandstone beds, with dark gray mudstone beds, interpreted as a flood dominated meandering system (Nakayama and Ulak, 1999). The Amlekhganj Formation is made up of salt and pepper, coarse to very coarse grained sandstones where the lower and middle members were interpreted as flood dominated meandering system and deeply sandy braided system, respectively (Nakayama and Ulak, 1999; Tamrakar and Khakurel, 2012). The Upper Amlekhganj Formation includes pebble-sized sandstones of a shallow sandy braided system (Nakayama and Ulak, 1999). The Churia Khola Formation was interpreted as a gravelly braided system consisting of cobble to pebble sized conglomerates, and the clasts are limestone and quartzite originating from the Lesser Himalaya (Nakayama and Ulak, 1999). Lastly, the Churia Mai Formation was interpreted as a debris flow braided system, comprised of poorly sorted boulder-sized conglomerates, some dark gray mudstones, and boulder-sized Siwalik sandstone clasts (Nakayama and Ulak, 1999).

Cross section studies of the Churia region include those done by Schelling et al. (1991) and Tamrakar and Khakurel (2012), which both focused on the area around Hetauda and Amlekhganj in Makwanpur as this area represents sections of each of the four lithological and geological formations (the Upper Member of the Rapti Formation, the Amlekhganj Formation, the Churia Khola Formation, and the Churia Mai Formation) and the

Quaternary fan deposits of the Terai. Figure 5 shows the cross sections from Schelling et al. (1991) and Tamrakar and Khakurel (2012). The cross sections show the flat plains of fluvial deposits that make up the Terai in the south, which is underlain by thick, flat, lying, middle Miocene to Pleistocene aged molasses of the Siwalik group (Schelling et al., 1991; Subedi et al., 2012; Tamrakar and Khakurel, 2012). In cross section, it is clearly visible that the Terai and Siwalik area represent the foreland basin of the Himalayas (Subedi et al., 2012).
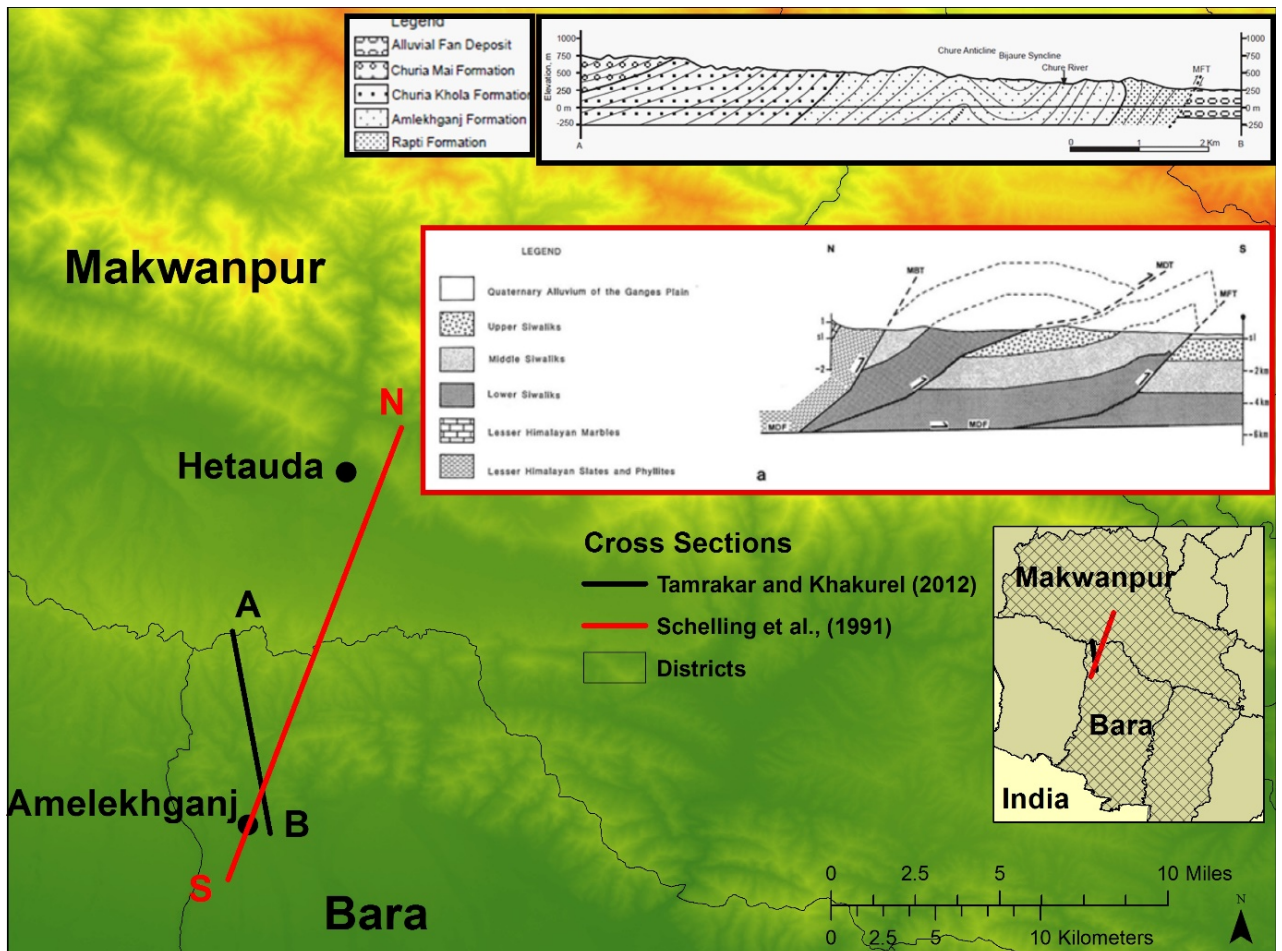
Figure 5. Central Nepal cross sections focusing on Hetauda to Amlekhganj. Compiled from Schelling et al. (1991) and Tamrakar and Khakurel (2012).

Other geological research in the Churia region has focused spanned geophysical studies (Gokarn et al., 2002), magnetic-polarity (Gautam and Appel, 1994, Gautam et al.,

15

2000), geometry and kinematics (Mugnier et al., 1999), watershed analysis (Honda et al., 1996), and oil and gas exploration studies (Subedi et al., 2012).

2.3 MONSOON

Panthi et al. (2015) studied rainfall trends from 1981 to 2012 in the Gandaki River Basin, which incorporates all five geological zones of Nepal. Data were examined during all four seasons (pre-monsoon, monsoon, post-monsoon, and winter). Monsoon rainfall has been increasing, especially in the Siwalik, while pre-monsoon, post-monsoon, and winter rainfalls have been decreasing (Panthi et al., 2015). The monsoon season has been lingering longer in recent years, which results in increased monsoon duration and increased total amount of annual precipitation, which suggests that there are more occurrences of intense precipitation, impacting agriculture and the livelihood for much of the population in the area (Panthi et al., 2015). The research found elevation and topography have active roles in the distribution of precipitation. The Tibetan Tethys zone receives the least precipitation, while the Siwalik and Terai zones receive the most annual precipitation. The research suggested that dry parts and seasons will become more dry as the decreasing trend in precipitation levels continues, while wet parts and seasons will become wetter (Panthi et al., 2015). Devkota (2014) examined climate change as it relates to monsoon precipitation in Nepal and found that rainfall has increased in the Churia region by more than 30mm/year.

Barros et al. (2000) modeled monsoon rainfall by studying the 1999 season in the mountains of central Nepal using rain gauge observations. The 1999 monsoon was reportedly a very intense season, and the data showed that even at 4000 masl the cumulative rainfall that year throughout the Indian subcontinent was record setting (Barros et al., 2000). Gillies et al. (2013) modelled monsoon precipitation in Nepal to forecast seasonal rain accumulation.

Nepal's monsoon precipitation shows distinct, strong, and typically decadal cycles (Gillies et al., 2013). Shrestha et al. (2000) also reported on the nearly decadal cyclic nature of monsoons as they used data from 1948 to 1994 to examine precipitation fluctuations throughout Nepal as it related to large scale climate parameters. The data showed distinct 11-year oscillation peaks in 1962, 1973 and 1984, and 1992 was the driest year in the entire record. The 1990-1994 data showed a downward trend consistent with the near 11-year cycle; however, the duration of the drop is longer than expected from the 11-year cycle alone, signifying that climate change is effecting monsoon precipitation (Shrestha et al., 2000).

2.4   FLOODS AND THE CHURIA REGION RIVERS

Syvitski and Brakenridge (2013) used remote sensing techniques to examine floods initiated during monsoon rainfall and exacerbated by dams, failures of irrigation/artificial levees, and sediment carrying capacity. Flow diversion is vital for effective flood control along sediment-rich and avulsion-prone rivers, such as those in the Churia region of Nepal (Syvitski and Brakenridge, 2013).

Shrestha et al. (2009) examined the weakly consolidated rocks with thin soil cover in the Churia River Basin and hydraulic parameters to determine the sediment carrying capacity of the river. The Churia river is intermittent as it appears only during intense monsoon rainfall (June–August) and otherwise is absent as a result of highly permeability (Shrestha et al., 2009). While the strength of the Churia rivers reduced downstream, they still had enough strength to move even the largest grain size during high rainfall levels (Shrestha et al., 2009). Any decrease in stream power was attributed to reduced slope, catchment area, boundary shear stress, and increased infiltration rates (Shrestha et al., 2009). To reduce the impact to

infrastructure downstream, sediment erosion management is paramount in the Churia region (Shrestha et al., 2009).

Tamrakar and Khakurel (2012) also studied rivers of the Churia River Basin in the Siwalik and Terai zones of Nepal. In general, the rivers have a sinuous appearance, which are typically sub-parallel, sub-dendritic, and occasionally rectangular as the rivers originate at higher elevations and spread out in the Terai as they travel south, carrying vast amounts of water and Quaternary sediment that then sculpt the landscape (Tamrakar and Khakurel, 2012).

2.5 LANDSLIDES

Bhandari et al. (2013) defined landslides as the movement of rock, debris, or soil caused by the action of gravity. In the Churia, the mass movement surface is typically shallow, and the landslide scar area typically small (Bhandari et al., 2013). Plummer et al. (2003) and Dahal et al. (2010a) classified landslides as translational, rotational, fall, or debris flows. Debris flows begin in small areas at the hilltop or gully head, tend to be shallow and activated by rainfall on slopes 30-40°, and flow with tremendous velocity that everything in the path is eroded and destroyed (Dahal et al., 2010a).

Focusing on the Siwalik Hill zone, Upreti (2001), Dahal et al. (2010a), Ghimire (2011), and Ghimire et al. (2013) assessed landslides and mass wasting, which are of constant concern in the zone, given the steep and unstable slopes (particularly the southern facing slopes), loosely packed, young, sedimentary rock, raised groundwater level, undercutting by rivers, and deforestation. More specifically, the conglomerates in the Upper Siwalik are loose, unconsolidated, and fragile, and in the Middle and Lower Siwalik, the alternating beds are vulnerable as the sandstones are easily weathered, as they are not well cemented, and the

mudstones tend to swell and flow when saturated with water, which results in overhanging

sandstone beds (Upreti, 2001; Dahal et al., 2010a; Ghimire, 2011; and Ghimire et al., 2013).

The numerous faults, thrusts, and folds of the Siwalik make this the most active zone of the

Himalayas (Upreti, 2001). Excessive rainfall is the most common trigger for landslides, but

earthquakes and artificial vibrations can also be the catalyst for landslides (Upreti, 2001;

Dahal and Hasegawa, 2008; Dahal, 2012).

2.6 NORMALIZED DIFFERENCE VEGETATION INDEX (NDVI)

Since the 1960s, scientists have been using remote sensing vegetation indices to study

plant vigor; the most commonly used index is the NDVI, which uses the near-infrared (NIR)

and red bands to measure vegetation intensity (Yengoh et al., 2014). As NDVI has been used

for decades, it has been applied throughout the world to study vegetation (Jackson and Huete,

1991; Barlow et al., 2003; Badamasi et al., 2012; Al-doski et al., 2013; Cao et al., 2014;

Johnston, 2014). Healthy vegetation reflects strongly in NIR section of the electromagnetic

spectrum, whereas unhealthy vegetation has a decreased reflectance. An NDVI raster output

will have values between +1 and -1. NDVI values closer to +1 indicate green, healthy

vegetation, bare soils and urban features will be closer 0, and water will negative values.

Equation 1 shows the formula for calculating NDVI.

Equation 1. NDVI

$$NDVI = \frac{(NIR - Red)}{(NIR + Red)}$$

2.7   LINEAMENTS

Lineaments are mappable linear features on the surface, which have a clear edge,

distinctly different in pattern and brightness from adjacent features (Caran et al, 1981;

Baumgardner, 1987; Argialas et al., 2003; Travaglia and Dainelli, 2003; Abdullah et al.,

2013). Imagery and algorithms such as PCI Geomatica's LINE module can be used to extract these linear features from a single band within an image and export the lines detected as a vector dataset. The LINE module also takes into account user-defined edge detection, thresholding, and curve extraction (PCI Geomatica, 2016). Lineaments are considered to have potential risk for landslides, as they represent planes of weakness. Numerous studies have successfully used remote sensing techniques to examine lineaments around the globe, including Greece (Papadaki et al., 2011), Malaysia (Abdullah et al., 2010; Ramli et al., 2009), the USA (Drahovzal, 1974; Kowalik and Gold, 1974; Caran et al., 1981; Shurr, 1982; Rodgers and Anderson, 1984; Baumgardner, 1987; Baumgardner 1991; McCulloh, 2003), Israel/Palestine (Mallast et al., 2011a; Mallast et al., 2011b), United Arab Emirates (Marghany and Hashim, 2010), Saudi Arabia (Qari, 2011), Yemen (Abdullah et al., 2013), Iraq (Thannoun, 2013), Afghanistan (Rahnama and Gloaguen, 2014), and Tunisia (Chaabouni 2012). Many previous studies have made use of Landsat, especially the shorter, short-wave infrared (SWIR) band, for lineament detection via the LINE algorithm as the band detects differences for soil, geological, and geomorphic purposes (Caran et al, 1981; Baumgardner, 1987; Argialas et al., 2003; Kocal et al., 2004; Marghany and Hashim, 2010; Muhammad and Awdal, 2012; Abdullah et al., 2013).

2.8   NORMALIZED DIFFERENCE MID-INFRARED (NDMIDIR) INDEX

Vohora and Donoghue (2004) and Mwaniki et al. (2015) used NDMIDIR to detect landslide scars in Landsat TM imagery. The NDMIDIR algorithm was initially designed to identify plant vigor beyond what NDVI was capable of monitoring and later for finding forest fire scars and landslide scars (Vohora and Donoghue, 2004; Mwaniki et al., 2015). The index uses the NIR and short-wave infrared (SWIR) band because the NIR band is highly

reflective for vegetation, and SWIR band is conducive for rock and soil studies (Vohora and Donoghue, 2004; Mwaniki et al., 2015). Equation 2 shows the formula for calculating NDMIDIR.

Equation 2. NDMIDIR

$$NDMIDIR = \frac{(NIR - SWIR)}{(NIR + SWIR)}$$

2.9   TEMPORAL CHANGE

Zhang and Xu (2008) and Xu et al. (2009) discussed and compared the strengths and weaknesses of the three types of change detection, image subtraction, image ratio, and change detection, using classification outputs, each of which provides the spatial distribution of features and qualitative and quantitative information of features changes.
Awasthi et al. (2002) used remote sensing and GIS techniques to measure land use change between 1978 and 1996. The results showed that agricultural lands in 1978 had been abandoned by 1996, which was attributed to increased out migration of the labor force. The change detection process quantified the degree to which the watersheds have suffered and continue to suffer from surface erosion and soil degradation (Awasthi et al., 2002). Baidya et al. (2009) conducted land use change analysis near protected lands in Nepal using imagery from 1978-1999 to assist in monitoring and modeling environmental change. The data were classified, NDVI outputs produced, and gross/net change calculated for each land use class. The results indicate that while forest management exists, vegetation degreased between 1978 and 1992, as the dominate class in 1978 was forest, but by 1992, the dominate class was agriculture (Baidya et al., 2009).

GIS data from 1958, 1978, and 1992 indicated that total forest area in the Churia hills study area was 81%, 72.9%, and 61.2%, respectively (Bhuju et al., 2007). The forest cover

had decreased by 25% and had become highly fragmented (Bhuju et al., 2007). Bhattarai et al. (2009) used Landsat imagery and linear regression models to measure deforestation in central Nepal using Landsat imagery from 1975-2000. Badamasi et al. (2012) used optical imagery from 1986 to 2005 to measure change using NDVI, land use classification outputs, and image subtraction methods.

Lane et al. (2003) used elevation data, photogrammetry, math models, and image differencing to quantify change in erosion and deposition to wide, braided, gravel-bed rivers between March 1999 and February 2000. Uddin and Shrestha (2011) also examined rivers by using GIS along with optical and radar data to monitor flood damaged in the Terai zone during the 2008 monsoon by using change detection techniques to quantity the extent of damage to lives and livelihoods by the catastrophic floods compared to imagery from 2000. Pradhan (2010) delineated flood risk using regression models, GIS data, and remote sensing techniques applied to optical and radar imagery. The data spanned 2006-2008 during monsoon rainfall and included land use maps, elevation data, and precipitation data.

2.10 LANDSLIDE RISK MAPPING

For more than two decades, research has been conducted to produce landslide hazard mapping in the Himalayas using geological weighted attributes (Pachauri and Pant, 1992; Honda et al., 1996; Pachauri et al., 1998; Pradhan et al., 2006; Dahal et al., 2008a; Dahal et al., 2008b; Bahadur, 2009; Ray and Smedt, 2009; Dahal et al., 2010b; Dahal et al., 2012; Bhattarai and Pradhan, 2013; Devkota et al., 2013; Kayastha et al., 2013; Poudyal, 2013), but none had focused on Bara or Rautahuat. Multi criteria evaluations of the spatial probability of landslides using weighted variables have been used to map landslides not only in Nepal but around the globe, including Switzerland (Metternicht et al., 2005), Italy (Mancini et al.,

2010), Turkey (Süzen and Doyuran, 2004; Akgun et al., 2012), USA (Weirich and Blesius, 2007; Tiwari and Douglas, 2012), Malaysia (Pradhan et al., 2008; Lee and Pradhan, 2006; Pradhan et al., 2009; Elmahdy et al., 2016), Thailand (Pantanahiran, 2005), Japan (Dahal et al., 2008c; Hasegawa et al., 2009b), Korea (Lee et al., 2012; Oh et al., 2012), and Bhutan (Singh et al., 2013).

Van Westen et al. (2006) discussed several methods for mapping landslide risk. One method uses weighted spatial probability modelling for landslide risk using GIS, tabular, remote sensing data, rankings, spatial analysis, and statistical analysis to provide quantitative risk assessment (Van Westen et al., 2006). The premise for quantitative landslide risk assessment is that the most important input is landslide data for previous landslide events, as these are vital indicators for the frequency and magnitude of landslides occurring in the future (Van Westen et al., 2006). Using weights of evidence modelling along with a knowledge-based approach has been widely used to classify the study area data as either high/moderate/low risk, as it offers a flexible way of testing the importance of input factors for landslide susceptibility (Van Westen et al., 2006). Previous landslide data is compiled with other datasets (lithology, slope gradient, slope aspect, curvature, distance from drainage, distance from faults, distance from infrastructure, geology, distance to lineaments, soils, precipitation, vegetation cover), using statistical methods to generate landslide susceptibility maps (Van Westen et al., 2006). Sarkar et al. (2006) summarized that there are two ways to calculate the weights, either use a subjective approach where expert knowledge is used to assign weights based on experience, or the option is to use a statistical approach where factors are correlated with landslide distribution. Not all variables involved in the final landslide risk model have the same influence on landslide occurrence (Sarkar et al., 2006).

The susceptibility model reflects the relative spatial probability of landslide occurrence to describe the relationship between the absence or presence of a landslide (Sarkar et al., 2006). Using a subset of the data used by Lee and Pradhan (2006), Figure 6 shows an example of the weighted spatial probability modelling method using slope and aspect layers. Each layer is divided into classes, and the total number and percent of all pixels of the study area in each of those classes is calculated. Next, the number and percent of known landslides occurring in each of those classes is calculated. Lastly, the frequency ratio for each class is calculated using the percent landslide occurrence to percent of pixels in the class. This ratio becomes the weight for that class.

Factor	Class	Total number of pixels		Landslide occurrence pixels		Frequency ratio
		Number[a]	%	Number[b]	%	
Slope	$0 \sim 15$ degree	1709800	57.87	53	11.45	0.20
	$16 \sim 25$ degree	765189	25.90	152	32.83	1.27
	$26 \sim 35$ degree	360229	12.19	157	33.91	2.78
	> 35 degree	119564	4.05	101	21.81	5.39
Aspect	Flat	1199400	40.59	13	2.80	0.07
	North	206629	6.99	41	8.85	1.27
	Northeast	207860	7.03	51	11.01	1.57
	East	228674	7.74	60	12.95	1.67
	Southeast	236988	8.02	82	17.71	2.21
	South	205108	6.94	58	12.53	1.80
	Southwest	206970	7.01	52	11.23	1.60
	West	228117	7.72	54	11.66	1.51
	Northwest	235036	7.95	52	11.23	1.41

Figure 6. Example of landslide risk mapping class weights. From Lee and Pradhan (2006).

CHAPTER THREE: METHODS AND MATERIALS

Initial processing of the SAR data used SENTINEL-1 SNAP freeware. Remote Sensing tasks were completed using Focus, EASI, Modeler, and OrthoEngine within PCI Geomatica suite version 2015. GIS work and geospatial tasks were completed using ArcMap version 10.3.1, ArcGIS® software by Esri. Ground truth points gathered in the field were collected using a Trimble Juno SD Handheld GPS unit. All spatial data were projected into UTM Zone 45N using WGS84 datum.

Figure 7 illustrates the remote sensing and tabular data and methods used. The optical data were orthorectified and atmospherically corrected before running the NDVI algorithm, NDIMIR algorithm, and unsupervised classification. The SAR data were orthorectifed and a speckle filter applied before running the flood detection process. Refer to Appendix A for an itemized table of the raster, vector, and tabular data used.
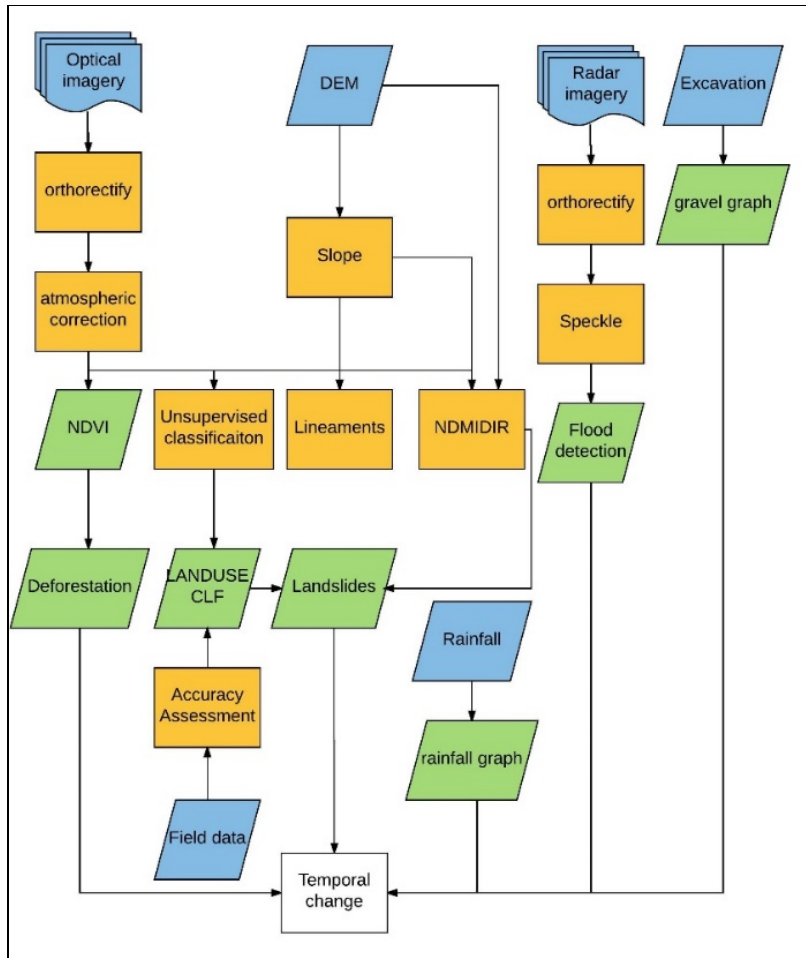
Figure 7. Remote sensing and tabular data and methods used.

3.1   FIELD WORK

Field observations were carried out in June-July 2014. Landslides and gravel excavation sites were visited, ground truth points were collected, and rock descriptions were made. Figure 8 shows the location of the points visited in Bara and Rautahat. These points represent 31 agriculture sites, 8 barren/bare sites, 27 urban/settlements sites, 27 forest sites, and 25 water sites. Sites were not visited in Makwanpur as it was not a known area of interest at the time of the field work.
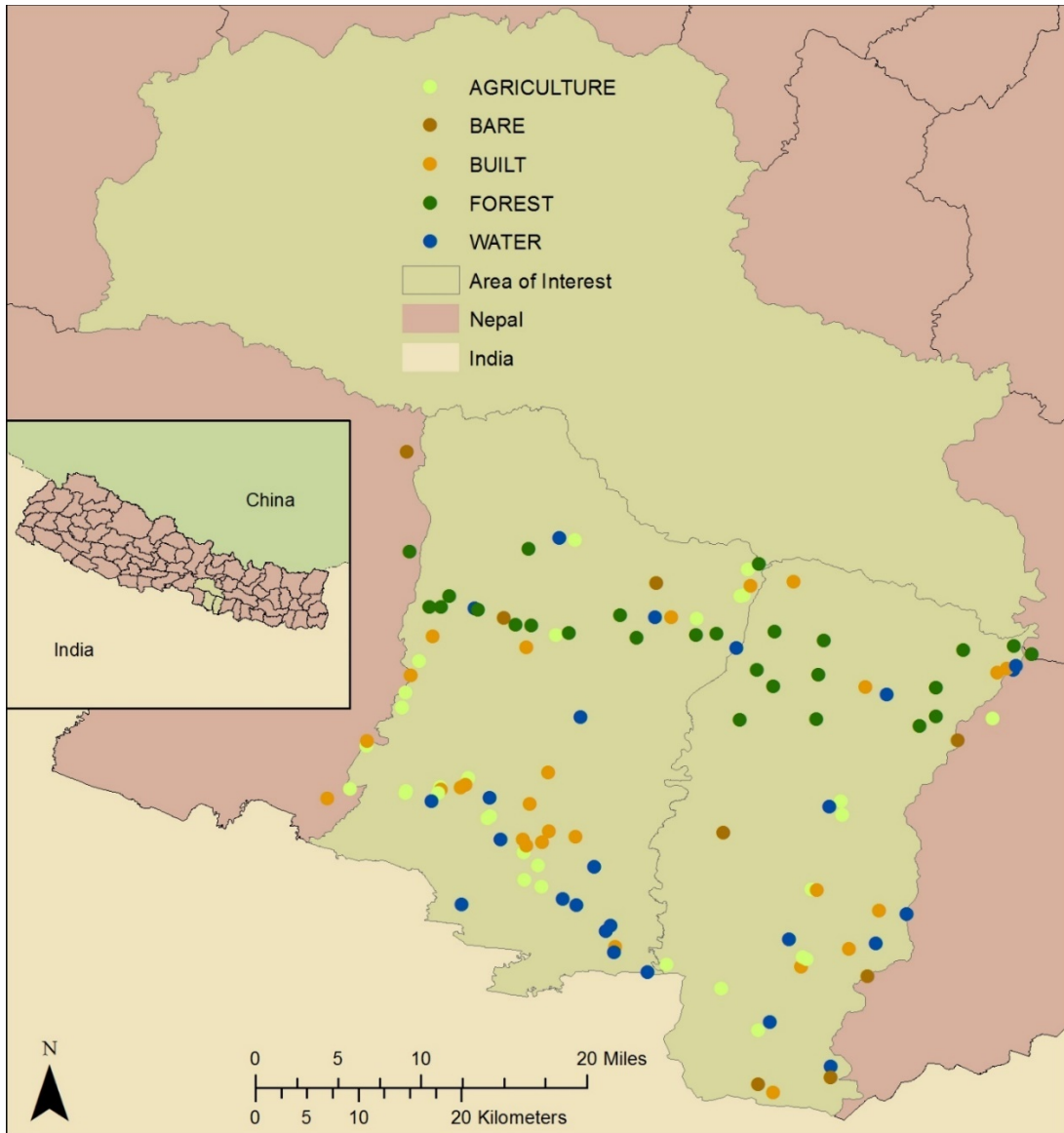
Figure 8. Field sites visited in Bara and Rautahat.

3.2   OPTICAL DATA

Table 4 shows the Landsat imagery and the purpose for which it was used. These

scenes are available for download from Earth Explorer, a data archives portal hosted by the

USGS. After being downloaded and bands compiled, the image from 1977 was orthorectifed

to align with the other images, and all images were atmospherically corrected to remove haze

using ATCOR, the proprietary atmospheric correction algorithm within PCI Geomatica.

Rectification errors of the 1977 image to the 2016 image were less than 0.5 pixels.

Table 4. Optical imagery used.

Sensor	Date (dd/mm/yyyy)	Path/Row	Purpose
Landsat 2MSS	27/10/1976	151/041	Classification
Landsat 2MSS	28/10/1976	152/041	Classification
Landsat 2MSS	1/6/1977	152/041	NDVI
Landsat 5 TM	6/6/1988	141/041	NDVI
Landsat 5 TM	12/10/1988	141/041	Classification, landslides
Landsat 5 TM	5/6/1999	141/041	NDVI
Landsat 5 TM	27/10/1999	141/041	Classification, landslides
Landsat 7ETM+	20/5/2002	141/041	NDVI
Landsat 5 TM	30/10/2006	141/041	Classification, landslides
Landsat 8 OLI	7/10/2015	141/041	Classification, landslides, Risk map
Landsat 8 OLI	18/5/2016	141/041	NDVI

NDVI was calculated using May/June Landsat images from 1977, 1988, 1999, 2002, and 2016. These scenes were chosen as they represent images with less than 10% cloud cover and leaf-on dates before crops were planted. The NDVI raster outputs representing forests were converted to shapefiles, and these polygons were used to calculate total forested area in the area of interest. The NDVI measurements represent 39 years of forest loss in the area of interest.

Unsupervised classifications using the IsoData Clustering (ISOCLUS) algorithm were created using October Landsat images from 1976, 1988, 1999, 2006, and 2015, using the visible, near infrared, and short-wave infrared bands. These dates were chosen as they represent images with less than 10% cloud cover, leaf-on dates, and dates where crops were not yet harvested. The classification raster outputs represented forest, agriculture, bare/barren soils, built area, water, and clouds. The outputs were converted to shapefiles, and the output polygons were used to quantify total land use area in the area of interest. The land use measurements represent 39 years of conversion of forest to urban/bare/agriculture in the area

of interest. An accuracy assessment was conducted on the 2015 land use classification and the ground truth points collected in the field.

A vector layer representing lineaments visible in a winter Landsat image from 26/12/2015 was created using the shorter SWIR band the LINE algorithm within PCI Geomatica.

The image used was chosen as it represented a recent, leaf-off image, with less than 10% cloud cover. Table 5 shows the parameters running the LINE algorithm.

Table 5. LINE parameters used

Parameter	Value
Line Radius (pixels)	10
Edge Gradient Threshold	100
Curve Length Threshold (pixels)	30
Line Fitting Error Threshold (pixels)	3
Angle Difference Threshold (degrees)	30
Linking Distance Threshold (pixels)	20

Landslide scar layers were created using the October Landsat images from 1988, 1999, 2006, and 2015 used to make the land use classifications. The 1976 October Landsat image was not used, as Landsat MSS does not include a short-wave infrared band necessary for running the NDMIDIR algorithm. For this study, the original NDMIDIR equation was modified to select NDMIDIR values ≤ 0.29, and elevations in the DEM > 450m, and slopes $>10°$, and not representing water or built areas in the 2015 classification. The landslide raster outputs representing landslides based on the relief, slope, NDMIDIR, and classification land use class requirements were converted to shapefiles, and these polygons were used to calculate total landslide area in the area of interest. The landslide measurements represent 27 years of landslide scars in the area of interest. The landslide polygons were validated against known landslides scar data created by the British Geological Society.

3.3   SYNTHETIC APERTURN RADAR (SAR) DATA

Table 6 shows the SAR imagery used. These scenes are available for download from the Vertex, a data portal hosted by the Alaska Satellite Facility (ASF), a NASA Distributed Active Archive Center (DAAC) and receiving ground station for SAR imagery. SENTINEL-1 Toolbox (S1TBX) freeware was used to radiometrically calibrate the data. A Refined Lee speckle filter was applied to each image to remove the salt and pepper appearance of interference. This speckle filter was used as it preserves edges while removing speckle (Veci, 2016). The SAR imagery was orthorectified to the 2016 Landsat OLI image, and the DEM was used to correct for geometry effects including shadow, foreshortening, and layover using OrthoEngine within PCI Geomatica. Rectification errors of the SAR imagery to the OLI image were less than 0.5 pixels.

Table 6. SAR imagery used

Sensor	Frame	Path	Date (dd/mm/yyyy)
JERS-1 SAR	383	18	28/07/1992
RADARSAT-1 SAR ST4	382	8	28/06/1998
RADARSAT-1 SAR ST4	67	330	20/07/1998
RADARSAT-1 SAR ST4	383	37	11/11/1999
PALSAR FBS	520 and 530	511	4/7/2007
PALSAR FBS	530	511	2/8/2007
PALSAR FBS	520 and 530	511	19/08/2007
PALSAR FBS	530	511	17/09/2007
PALSAR FBS	520 and 530	511	4/10/2007
PALSAR FBS	520 and 530	511	6/7/2008
PALSAR FBS	520 and 530	511	21/11/2008
Sentinel 1A	85	83	16/05/2015
Sentinel 1A	19	501	28/06/2015
Sentinel 1A	85	83	2/7/2015
Sentinel 1A	19	501	10/7/2015
Sentinel 1A	85	83	14/07/2015
Sentinel 1A	19	502	22/07/2015
Sentinel 1A	85	83	26/07/2015
Sentinel 1A	85	86	31/08/2015
Sentinel 1A	85	85	6/10/2015
Sentinel 1A	19	502	10/6/2016
Sentinel 1A	85	85	20/07/2016
Sentinel 1A	19	507	28/07/2016

Initially, CHDET, the proprietary algorithm within PCI Geomatica to detect change between two SAR amplitude, was used. However, there was not enough significant flooding to make use of this algorithm. Instead, total wetness in each SAR image was calculated based on the histogram range for very dark and smooth pixels. The "wetness" raster outputs representing water were converted to shapefiles, and these polygons were used to calculate total water area in the area of interest. These polygons were then subtracted from the published river shapefile, and the output was considered to be unexpected waterbodies. Upon closer examination of the main rivers in the AOI using Google Earth, it was discovered that there are dams, hydroelectric structures, irrigation, and divergent features built as

recently as 2001, if not earlier. This helps to explain why the rivers did not produce significant flooding as initially expected.

3.3 DIGITIZED DATA

The data available online for download pertaining to thrust, faults, and geology for Nepal was too generalized and the accuracy questionable; thus, thrusts, faults, and geological maps were digitized using scanned journal articles figures (Nakayama and Ulak, 1999; Upreti, 1999, Tamrakar and Khakurel, 2013; Syangbo and Tamrakar, 2013), a scanned geological map (Department of Mines and Geology, 2011), and the georeferencing using the rubber sheeting method within ArcMap.

3.4 LANDSLIDE RISK MAP

Figure 9 shows the layers and work flow used to create the landslide risk map. Layers used include rivers, settlements, thrusts and faults, landslides, lithology, precipitation, roads, DEM, slope, aspect, NDVI, geology, lineaments, and land use classes. If not already applied, the input layers were clipped to the AOI and converted to UTM Zone 45N using WGS84 datum; some layers were converted to density rasters, and others were buffered and then converted to raster. Once all layers were converted to rasters, thresholds were applied, and the layers were ranked as part of the weighted sum process to produce the landslide risk map. Refer to Appendix B for specific buffer distances, reclassification thresholds, and overall layer ranks used for the final weighted sum landslide risk map output.
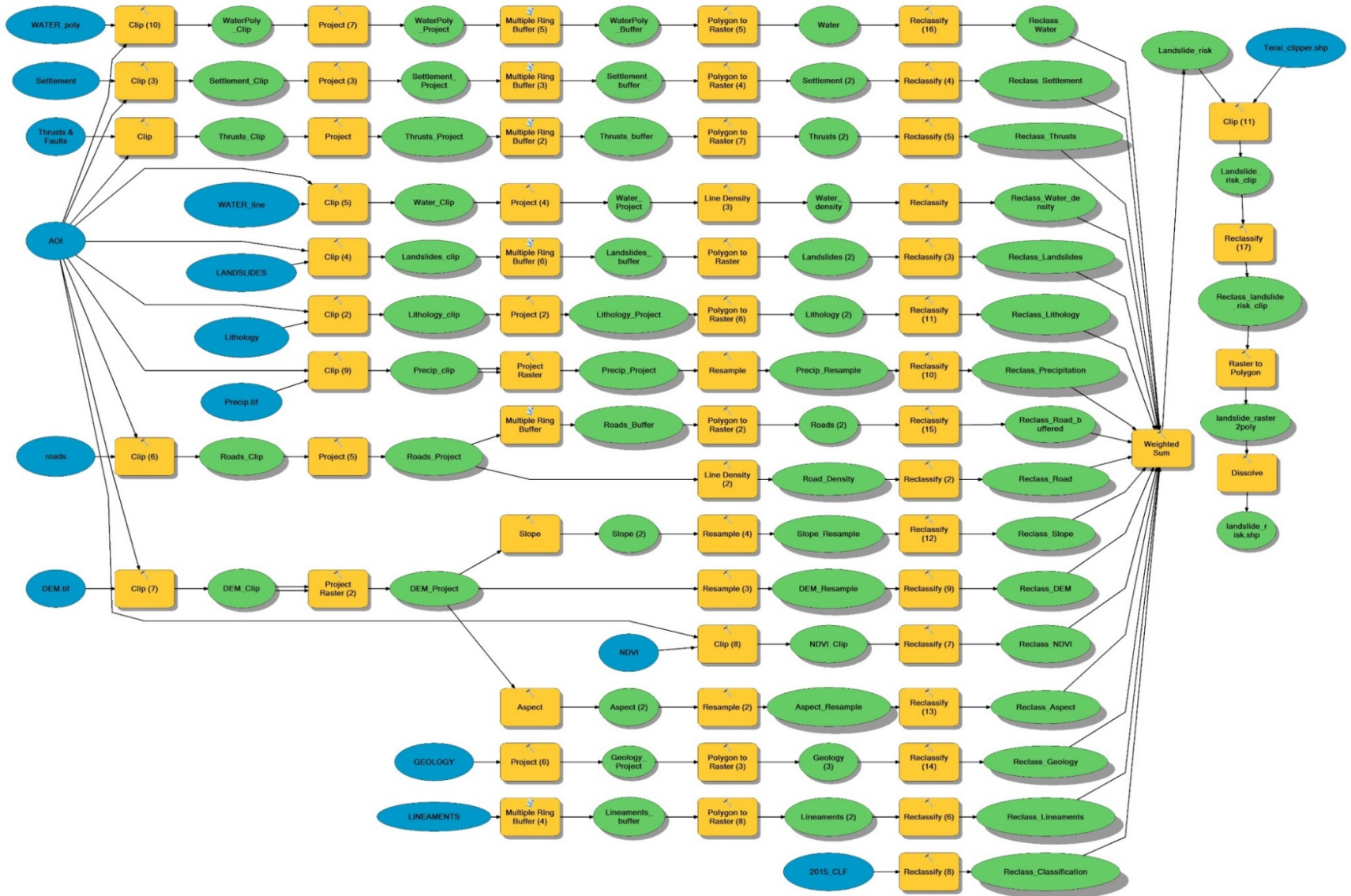
Figure 9. Landslide risk map work flow.

3.4   GRAVEL EXPORT DATA AND PRECIPITATION DATA

Excavation data from 2001-2011 regarding sand, gravel, rocks, and minerals were procured from the Department of Customs, Central office, Kathmandu, Nepal, representing data collected at the Birgunj, Nepal border crossing. This data was transposed to Julien calendar dates and converted to tons, so the data is in all in a common unit of measure. Only data defined as "gravel less than 2 inches in size" were considered for this study. Precipitation data for 2001 to 2012 was extracted from the Central Bureau of Statistics for Simara Airport in Bara and Hetauda in Makwanpur (Central Bureau of Statistics, 2013). Similar data for Birgunj spanning 1974 to 2013 from the Department of Hydrology and Meteorology, Kathmandu, Nepal was provided by Asta-Ja Research and Development Center in Kathmandu, Nepal.

CHAPTER FOUR: RESULTS

This chapter includes results from the field work and geospatial processes.

4.1   FIELD DATA

Figure 10 shows a section of cut bank along the Dudhaura River as an example of the typical alluvium on top of gravel sediments at rivers in the study area. Starting at the base there was approximately one meter of gravels, pebbles, and fine sand, above which is a 12cm layer of visible roots and vegetation, pebbles, and fine sand. At the surface, fine grain sands and dark organics of the soil profile visible. The courser grains indicate rapid channel deposition, while the finer grain material indicates a slower depositional environment along a point bar of a meandering stream.
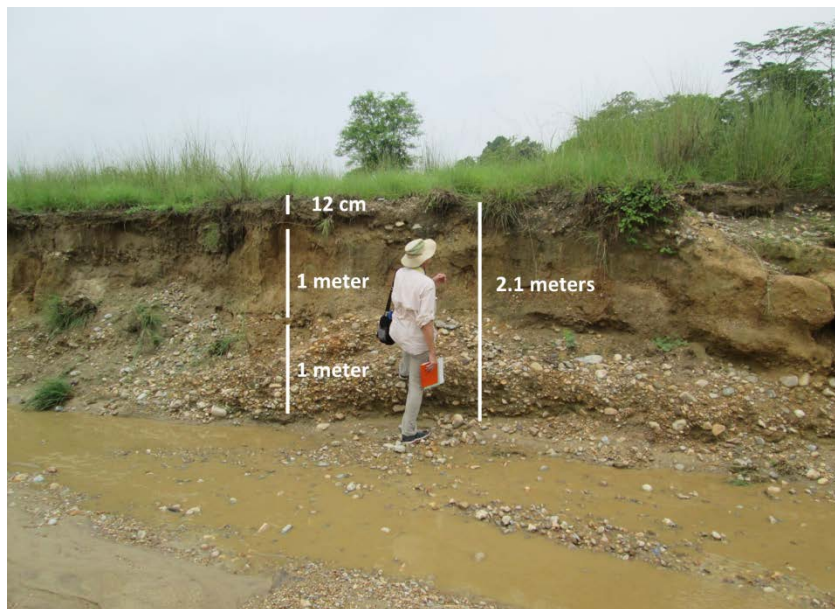
Figure 10. Cut bank along the Dudhaura River.

Figure 11 shows cobbles in the river bed at the Dudhaura River. Most pebbles were generally semi-rounded and approximately 6-cm in size; the largest pebbles appeared to be 15-cm in size. The river bed consisted of gravel, sands, silt, and mud.

Figure 11. Pebbles in the river bed at the Dudhaura River.

Figure 12 shows a sedimentary rock sample in the Dhansar River close to the Dhansar

Bridge that represents the young and easily eroded sandstones of the Siwalik, deposited here

in the Terai by the rivers. Figure 13 shows the same rock material farther upstream in the

Siwalik region. The size of these sandstone boulders clearly shows the massive power the

river must have during peak Monsoon season in order to move this massive weight. The

distance between the location of the rock sample in Figure 12 and Figure 13 is 8.5km, and

the elevation difference is 166 meters.

Figure 12. Sedimentary rock sample that represent the Siwalik, deposited in the Terai by the Dhansar River.

Figure 13. Sandstone boulders in the Siwalik.

The sedimentary formations are unique to the Siwalik, as the rest of the Himalayas are metamorphic and igneous. Figure 14-16 represent outcrops in the Lower Siwalik but within approximately 200m from the boundary of Lower Middle Siwalik. The rocks are fine to medium grained sandstone interbedded with siltstone and mudstone. Figure 14 shows a

sandstone outcrop interbedded with shale. The beds are dipping nearly due North at 20º; this location is at the north flank of an anticline and less than 500m north of the massive boulders shown in Figure 13.

Figure 14. Sandstone outcrop anticline.

About 100m further north, the massive sandstone beds are on top of finer grained shale and mudstone. The beds have flattened out essentially at the boundary of the Lower Siwalik and the Lower Middle Siwalik (Figure 15, top). The easily eroded nature of the sandstone beds is evident by the step-like appearance in the riverbed (Figure 15, bottom).

Figure 15. Horizontal sandstone and shale/mudstone beds.

Figure 16 shows a pinch out of the massive sandstone beds on top of predominately horizontal shale and mudstone bedding. The structure was deposited by the river. The area had several units of thickening and thinning layers. Strike and dip measurements were not recorded here, as there was significant variation in the orientation of the beds.

Figure 16. Pinch out of sandstone beds on top of shale/mudstone.

Landslide scars are responsible for having tremendously reshaped the geography of the Churia region and the unstable terrain and steep valleys are at the mercy of the force and destruction of these landslides (Dahal et al., 2006). Figure 17 illustrates the mass movement common to the study area. The movement begins as slope failure in the upper reaches of the landslide impact area, a slump starting at a fault becomes triggered, material slides until a rotational component is introduced, causing the path to curve (Dahal et al., 2006). The movement becomes a debris flow when the material becomes a mix of sediment and flow (Dahal et al., 2006). Oftentimes, the landslide spreads laterally, significantly increasing the impacted area and ultimately generating a low angle and board landslide mass (Dahal et al., 2006). Figure 17a shows a concave area now covered with vegetation; the area immediately below shows a mound of material also covered by grass, which represents the moved material. Figure 17 (b and c) show the curved path of the landslide.
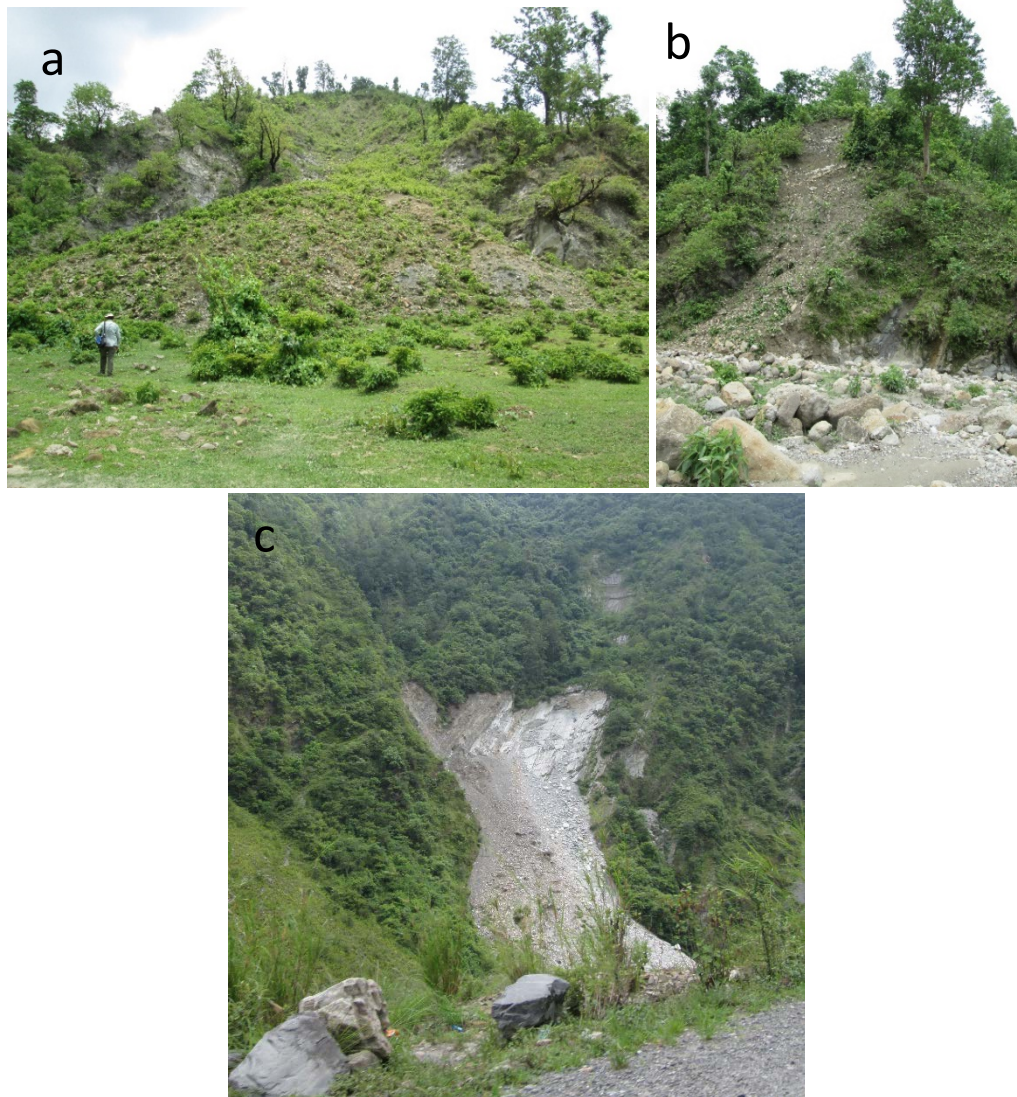
Figure 17. Mass movement in the study area begins as a slump, the path curves, and the movement becomes a debris flow.

The gravel data procured from the Department of Customs, Central Office,

Kathmandu, Nepal representing data collected at the Birgunj, Nepal border crossing shows

that during the first year of data collection, in 2001-2002, over 800,000 tons of gravel export

was documented. In the following two years, exports increased to nearly 1.7 million tons.

Exports continued to increase through 2008. A dramatic increase in gravel exportation took

place between 2004-2005 to 2007-2008 when exports peaked at 6.15 million tons.

Conversely, between 2008-2010, there was a significant decrease in reported gravel exports,

which continued through 2010-2011 (Figure 18). The data represent gravel excavation

records from a single border crossing between Birgunj, Nepal and India.
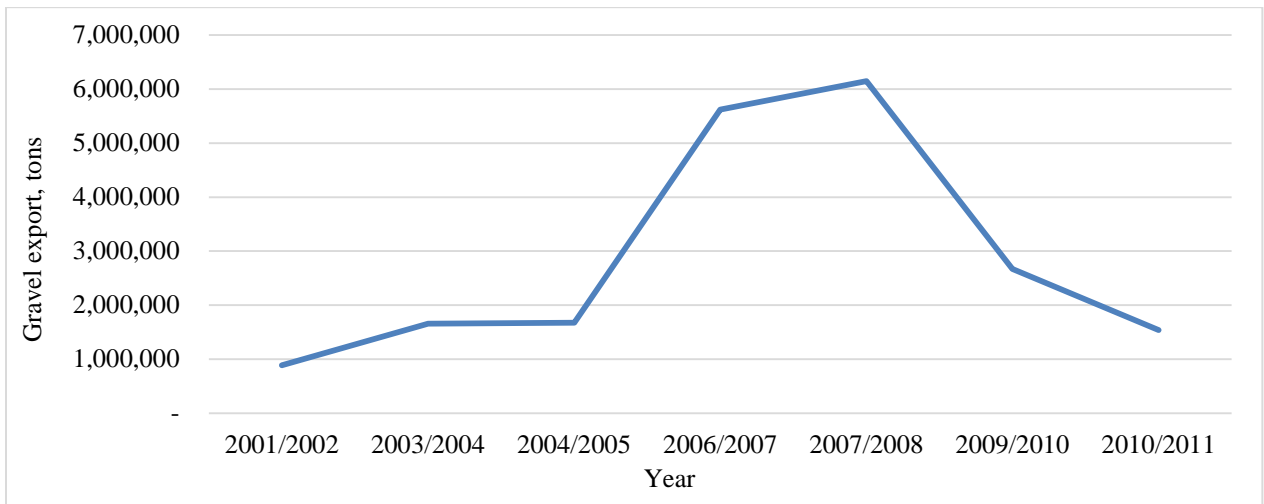
Figure 18. Gravel excavation records from the Birgunj, Nepal border crossing, 2001-2010.

The extent to which stone quarrying has exacerbated the Churia degradation process

is clear. Figure 19 (top) shows that gravel excavation is wide spread, unregulated, and

disastrous across each river valley of the Terai. Hundreds of trucks line along the roads

connecting Nepal to India daily, waiting to cross into India, loaded with excavated gravel

(Figure 19, bottom).

Figure 19. Trucks get filled with excavated gravel (top) and line up to cross into India to deliver the gravel as construction material (bottom).

4.2   PRECIPITATION DATA

The rainfall data spanning 1974-2013 for Birgunj shows that nearly all the rainfall the

region experiences takes place during the monsoon season (June - September). Figure 20

shows the monthly average rainfall recordings for the city of Birganj spanning 39 years. Most rainfall takes place in July with an average monthly accumulation of 465 mm. Conversely, the driest month is typically November, which has an average monthly accumulation of merely 7 mm.
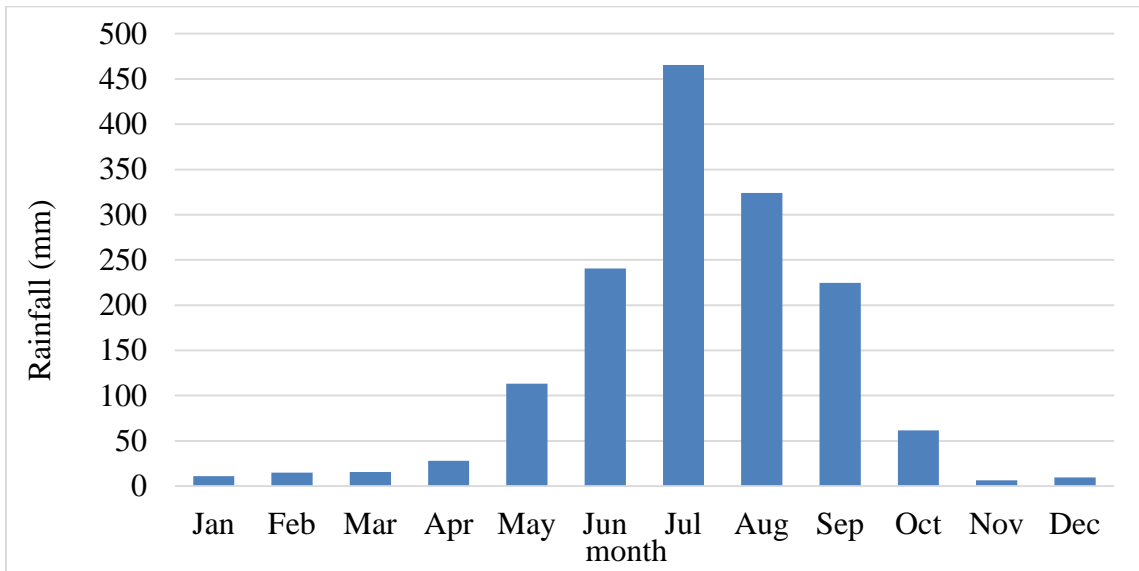
Figure 20. Monthly average rainfall (mm) for Birgunj, Parsa between 1974-2013.

Figure 21 shows that total annual precipitation in the Terai (Birganj and Simara) ranges from 815 mm at Birgunj to nearly 3000 mm in 2007 in Simara. Precipitation in the hills (Hetauda) peaked in 2002 with over 3300 mm of rain, while the driest year was 2012 with just 1626 mm of rain. The data at all three weather stations shows that 2007 was a uniquely rainy year.
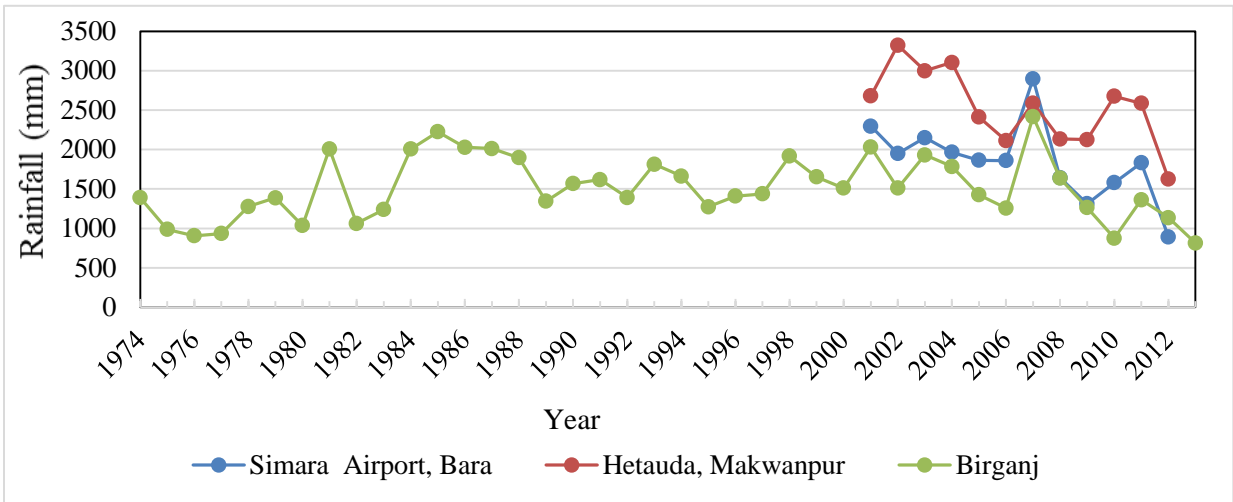
Figure 21. Annual Rainfall measured at Simara Airport in Bara, Hetauda in Makwanpur, and Birgunj in Parsa between 1974 to 2013.

When comparing the annual precipitation levels where the three measuring stations overlap, the 2001-2012 precipitation data indicate that rainfall levels are in a cycle of decreased rainfall (Figure 22). This decrease could illustrate the decadal cyclic nature of monsoons and simply represent a section of the 11-year oscillations discussed by Shrestha et al. (2000). Hetauda almost always has higher precipitation than Simara or Birgunj (Figure 22). Average annual rainfall at Simara and Birgunj compared to Hetauda is 1853 mm and 1511 mm compared to 2530 mm, respectively.
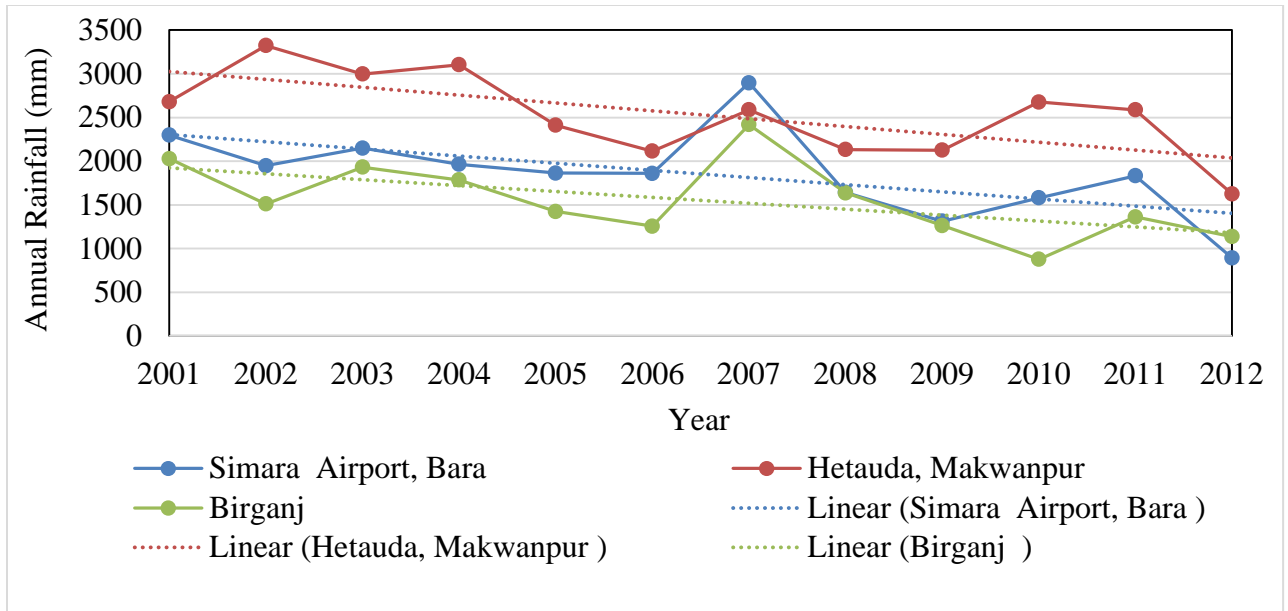
Figure 22. Annual Rainfall measured at Simara Airport in Bara, Hetauda in Makwanpur, and Birgunj in Parsa between 2001-2012.

4.3   OPTICAL DATA

The NDVI results show that between 1977 and 2016, 1,812 km^2 of forest were removed (Figure 23). This represents an average rate of 1.03% loss per year, which is close to the national average of 1.2-1.7% deforestation per year (Chakraborty, 2001; Gautam et al., 2004; Kandel, 2009; Rastrapati Chure Conservation Program, 2013). In 1977, the study area consisted of 3,310 km^2 of forest cover, which represented 70% of the area of interest. Forest cover decreased steadily from 1988 to 2002 from 60% forest cover to only 51% forest. Between 2002 and 2016, there was a dramatic decrease in forest cover, which dropped to merely 1,498 km^2 or 32% of the study area.
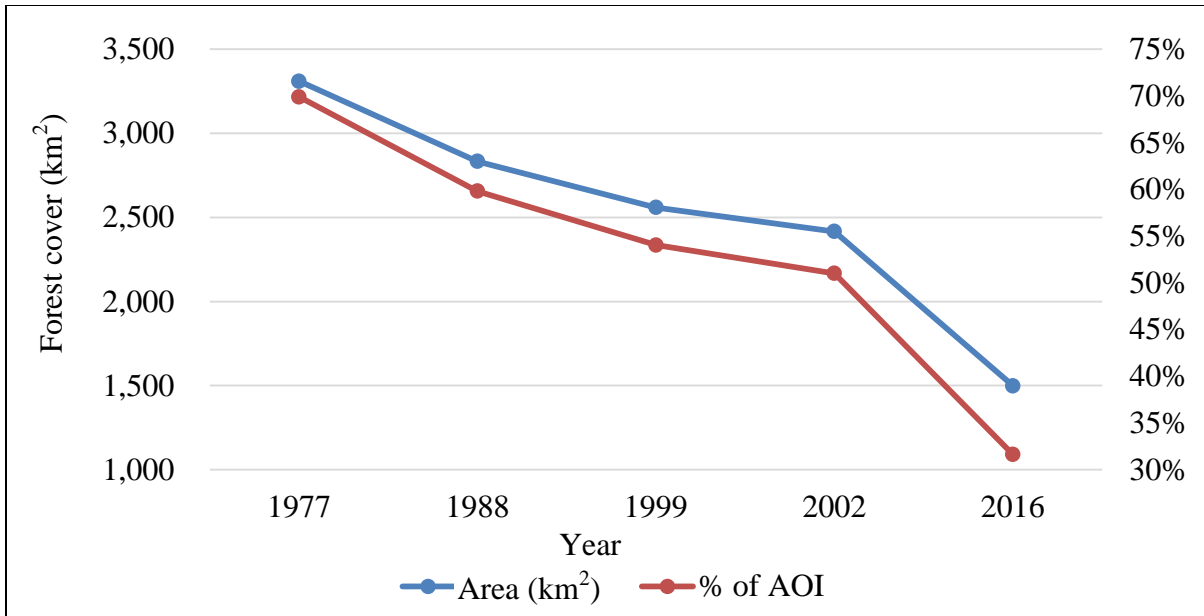
Figure 23. Forest cover decline in the study area between 1977-2016.

Figure 24 shows examples of forest cover decline in three sections of the study area over nearly four decades. The imagery in the background is the respective Landsat scene. The black outlined area shows forest loss around Hetauda. In Bara, the area outlined in blue shows vegetation transition from forest to agricultural land, while the yellow outlined area shows urbanization between Bhaudaha, Kakadi, and Parsauni. In Rautahat, the pink and green outlined areas show significant transition from forest to settlement and forest to agriculture, respectively.
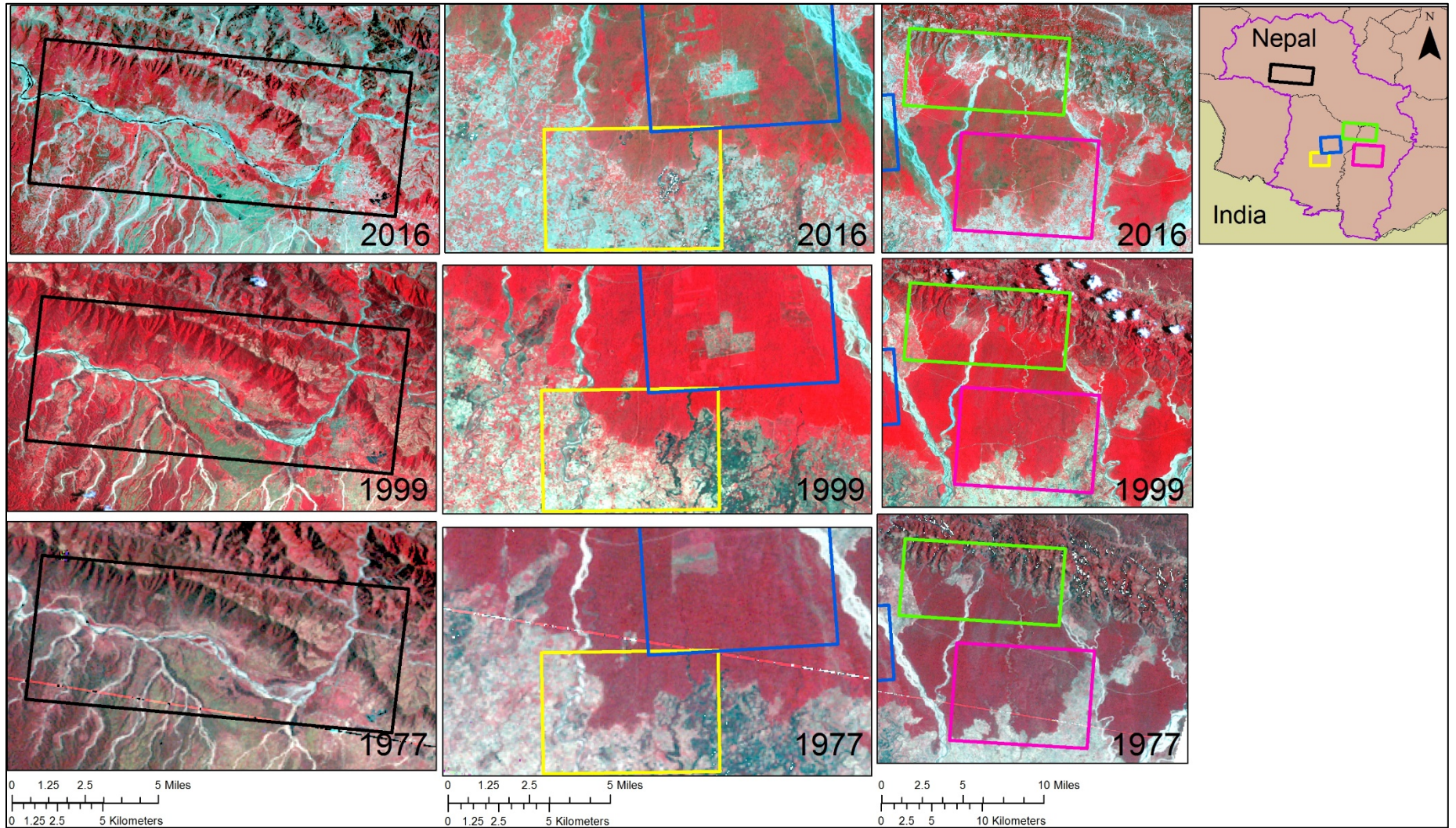
Figure 24. Landsat imagery showing forest cover decline in the study area between 1977-2016.

The results from the unsupervised classifications also showed significant transformation from forest to other land use types (built areas, bare soil, and agriculture). Figure 25 shows that agriculture, bare soils, and built landscapes have increased at the expense of forest cover over the last 40 years.
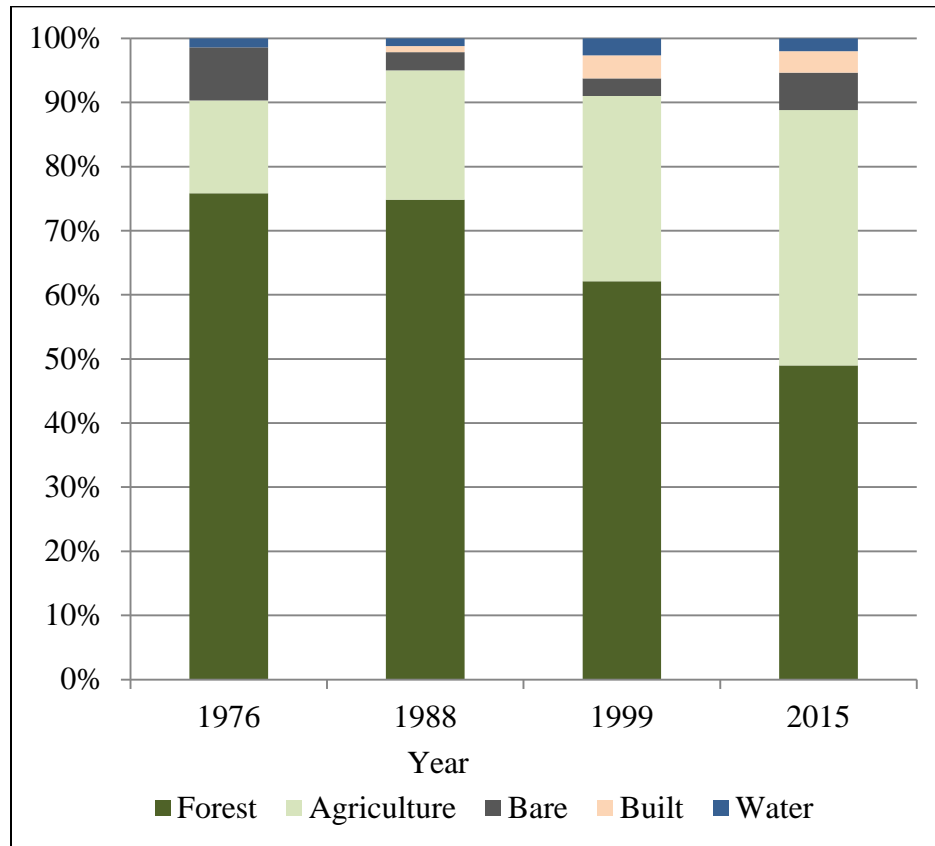
Figure 25. Land use change in the study area from 1976-2016.

The overall accuracy of the 2015 classification was 79%. Table 7 shows the accuracy agreement between the classification output and the ground truth points collected in the field. Values highlighted in yellow represent sites which were classified correctly, with the remaining values representing sites incorrectly classified according to the reference data. The classification mapped forest, agriculture, and water acceptably well. The classification satisfactorily mapped bare soil and built landscapes.

Table 7. 2015 Classification Accuracy Assessment.

| Classification | Ground Truth Points | | | | | TOTAL | User's Accuracy |
	Forest	Agriculture	Bare	Built	Water		
Forest	30	2	0	0	0	32	94%
Agriculture	0	29	5	7	1	42	69%
Bare	0	0	16	4	3	23	70%
Built	0	0	3	18	0	21	86%
Water	0	0	6	1	26	33	79%
TOTAL	30	31	30	30	30	151	
Producers Accuracy	100%	94%	53%	60%	87%		
Overall classification accuracy							79%

The user's and producer's accuracy were given for each class to further show the accuracy of the 2015 classification. User's accuracy shows the reliability of classes in the classified image. The calculation represents the ratio of correctly classified pixels with regards to all pixels classified as a specific class in the classified image (Lillesand et al., 2015). As an example, for the Forest class, the reliability is 30/32 = 94%, meaning that approximately 94% of the Forest pixels in the classified image actually represent forest on the ground. Producer's accuracy shows the accuracy of the classification. The calculation represents the ratio of correctly classified pixels in relation to all pixels of that ground truth class (Lillesand et al., 2015). As an example, for the Water class, the producer's accuracy is 26/30 = 87%; this shows that approximately 87% of the water ground truth pixels also appear as water pixels in the classified image. The user's and producer's calculations specify how the classification model output varies across classes, and output is summarized by the Kappa (κ) coefficient, where results < 40% are weak and results ≤ 80% are ideal (Lillesand et al., 2015). The Kappa coefficient for the 2015 classification is moderately good, as κ was 73%.

The results of the modified NDMIDIR algorithm indicated that there has been a general increase in area impacted by landslides between 1988-2016. Table 8 shows the total area impacted by landslides in Bara, Rautahat, and Makwanpur districts between 1988-2016 using the modified NDMIDIR algorithm. To validate the NDMIDIR outputs, the landslides where compared against the 78 landslides identified by staff at the British Geological Society and Durham University immediately following the 2015 Nepal Earthquakes using airphoto interpretation (Durham University, 2016). Fifty-four of the 2015 NDMIDIR landslides were within 1-pixel width (30m) of a landslide defined by the British Geological Society. Eight-five percent (66 of 78) of the Durham University and British Geological Society's landslides were within 500 meters of 2015 NDMIDIR landslides. The creators of the Durham University and British Geological Society's landslide dataset note that precise landslide locations may be inaccurate by up to 100 m (Durham University, 2016).

Table 8. Total area impacted by landslides between 1988-2016 using the modified NDMIDIR algorithm.

Year	1988	1999	2006	2016
Area total (km²)	7.26	7.7	7.49	8.73

4.4   SAR DATA

The results of the river inundation work were inconclusive. Not only did the rivers not produce the flood inundation anticipated, but the SAR data showed that the rivers rarely, if ever, fill the entire river bed. Figure 26 shows the locations where river widths were measured. The rivers were rarely, if ever, as wide as their corresponding topographic map shapefile riverbed widths. Figure 27 also shows that river width measurements were inconclusive. Explanations for this lack of anticipated river inundation are described in the discussion section of this thesis.

51
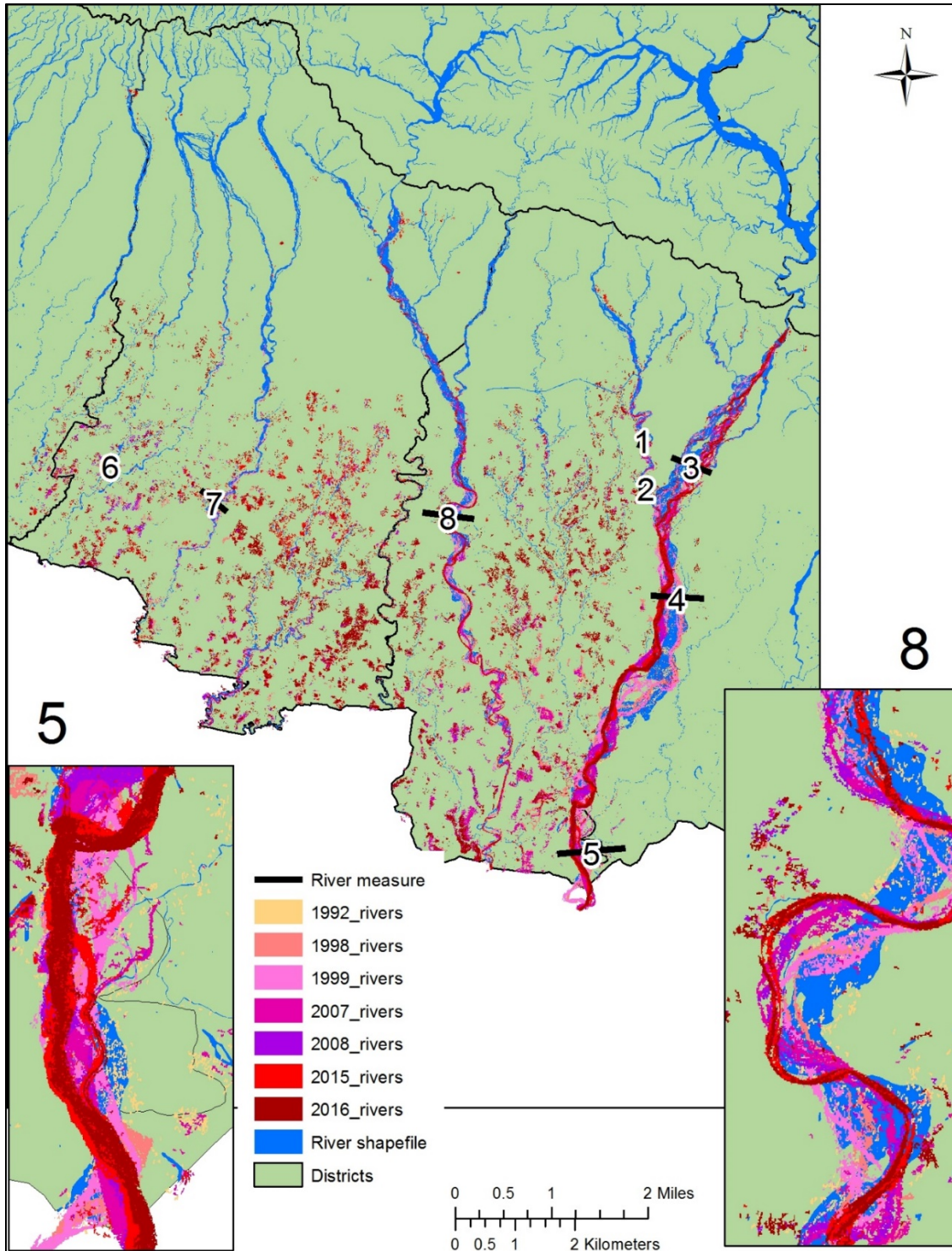
Figure 26. Rivers within the study area.
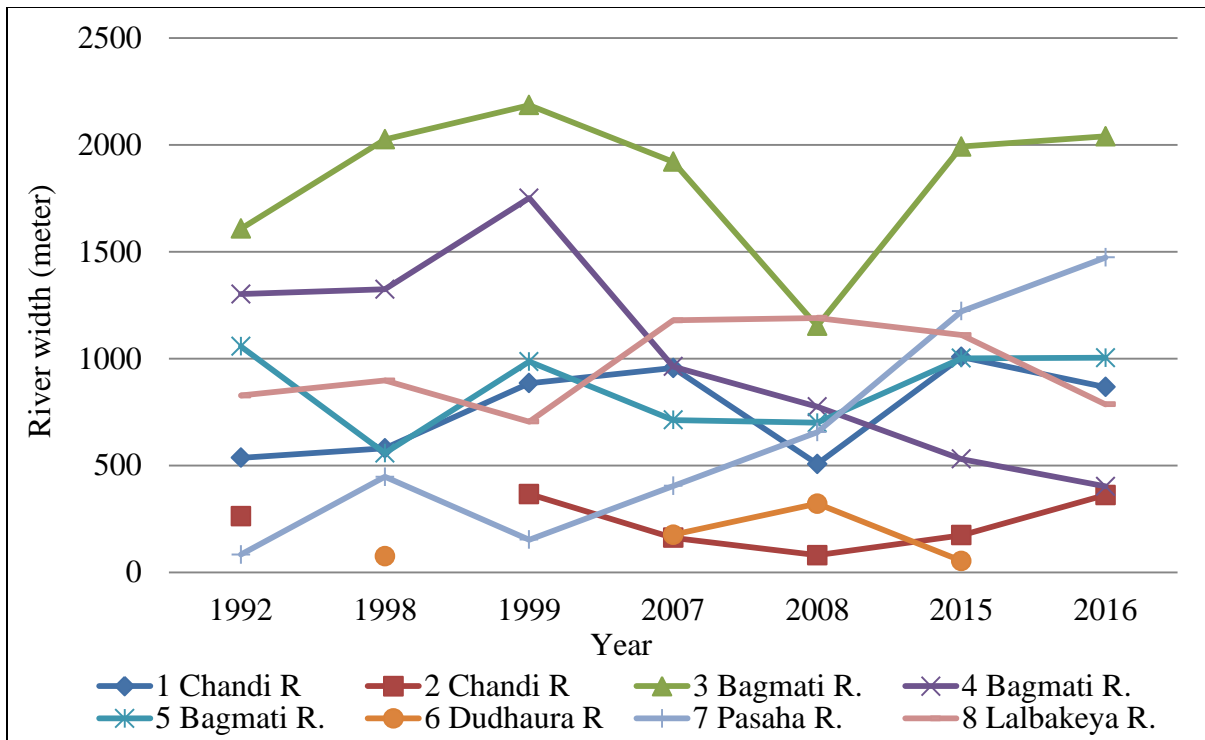
Figure 27. Selected River Width Measurements throughout the study area.

Conversely, it was found that water does pool in the lowlands of the study area, as one would expect of a flood plain. Figure 28 shows water pooling in the flood plain more so in recent years than in the past. The data shows that rain water accumulation has increased from 1992 to 2016 from 7.97 km^2 to nearly 50 km^2. Both 1999 and 2008 appear to be outliners; this could be attributed to not having full imagery coverage for the entire study area during these years. Data for 1992 also did not cover the full study area.
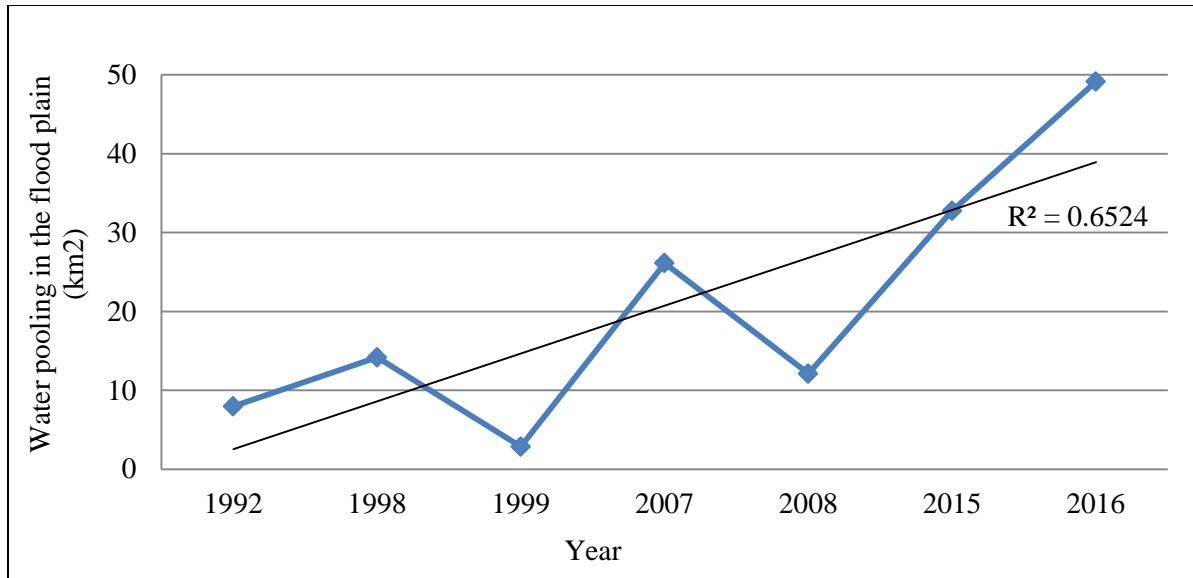
Figure 28. Total area of accumulated water (possible flood water) detected in the SAR imagery.

4.5 DIGITIZED DATA

Over 600 lineaments were generated by the LINE algorithm within PCI Geomatica and ranged from 67-5,000 meters. Most of the lineaments where approximately 1,100 meters in length. Most of the lineaments were oriented in NE-SW direction; some were N-S and NW-SE. These features represent tectonically weak areas and potentially identify deep fracture zones or faults, which delineate areas of possible instability and landslide risk (Caran et al, 1981; Baumgardner, 1987; Argialas et al., 2003; Travaglia and Dainelli, 2003; Abdullah et al., 2013).

4.6 LANDSLIDE RISK MAP

Figure 29 shows the output map of the landslide risk model. The Terai was not included in the final landslide risk map or risk calculations as the elevations, slopes, and risk values were very low. Table 9 shows that nearly 70% of the Siwalik hills in the study area and far south section of the Lesser Mountains have moderate to very high risk of landslides.
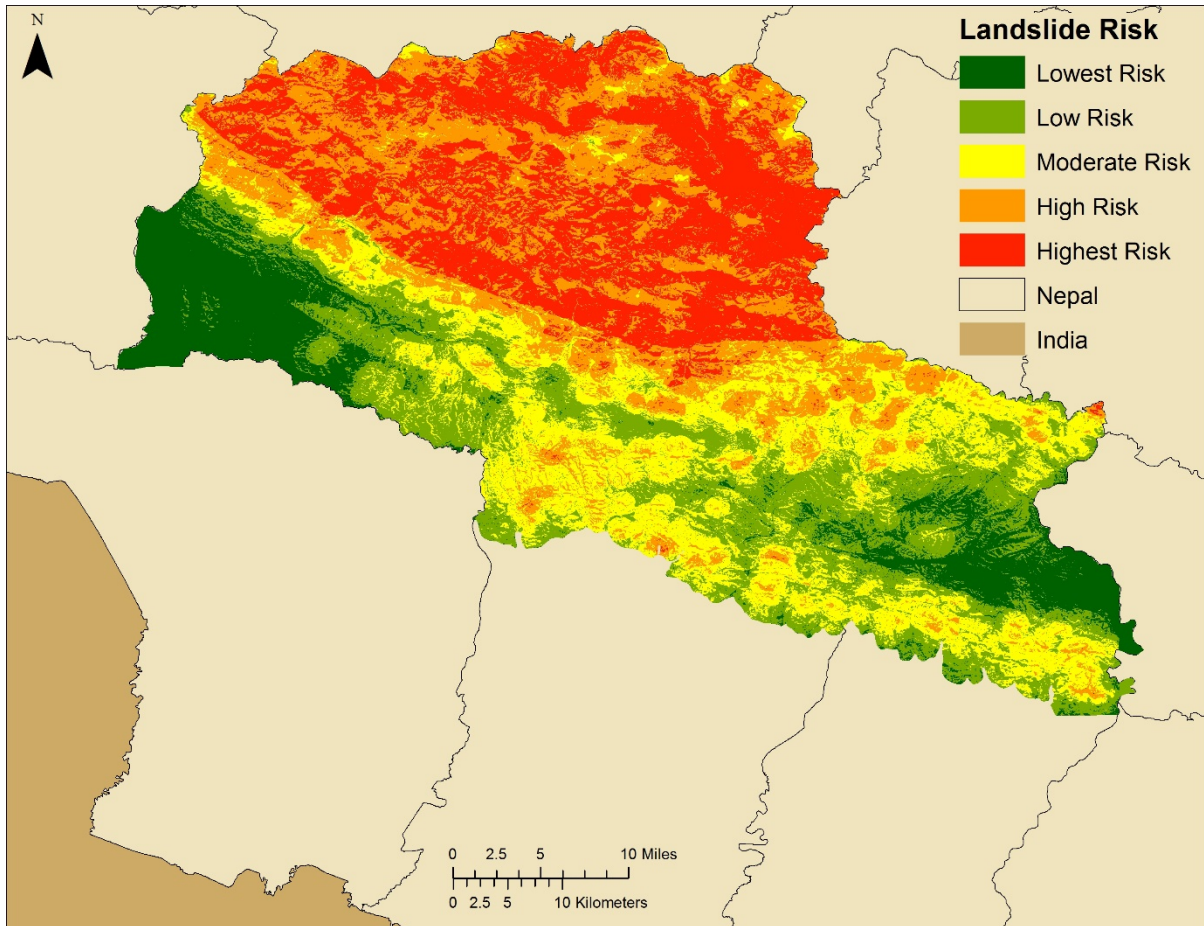
Figure 29. Map output from the model created to assess landslide risk.

Table 9. Landslide risk map results in the Siwalik and southern Lesser Himalayan zones.

Landslide Risk	Area (km^2)	Percent
Lowest Risk	286.3	10.9%
Low Risk	528.6	20.1%
Moderate Risk	582.2	22.2%
High Risk	609.3	23.2%
Highest Risk	620.8	23.6%

CHAPTER FIVE: DISCUSSION

This chapter discusses the following: (1) temporal change of landslides in the Churia region correlated with temporal changes in land use/deforestation/urbanization in the region, (2) temporal change of river inundation in the Terai and the extent to which river inundation exacerbates the Churia degradation process, (3) the extent to which stone quarrying exacerbates the Churia degradation process, and (4) the implications of the landslide hazard risk map.

5.1 FIELD OBSERVATIONS

A clear example of degradation of the Churia region due to gravel excavation was observed at the intersection of the Dudhaura River at the East-West Highway, where more than two meters of gravel has been removed over the last 40 years. Figure 32a shows a cross section sketch of the terraces adjacent to the river, which show the current and previous river levels. The large trees represent the original terrace, the smaller trees and shrubs indicate the second terrace, and the grasses show the current peak river levels. The bridge and mature trees date to more than 40 years ago, when the highway and bridge were built. Locals report having planted the younger trees on the lower terrace 15 years ago. The original water line can be seen stained on the bridge pillars (Figure 32b). Locals reported that gravel mining began at least 22 years ago. Laws against excavation within 200m of the bridge have not been enforced and have undermined the stability of the bridge. Originally, tall trucks excavating gravel years ago were too tall to pass under the bridge. Lowering the stream has increased the gradient of the river, which has increased water velocities, resulting in higher load carrying potential. The stream adjusts to the depth change by eroding the banks. The river will continue to cut deeper so long as gravel excavation continues. According to locals,

in recent years during monsoons, the water velocities are so high that eddies around the

bridge pillars occur. Figure 32c shows an annotated field photo showing the terraces and

vegetation adjacent to the river.
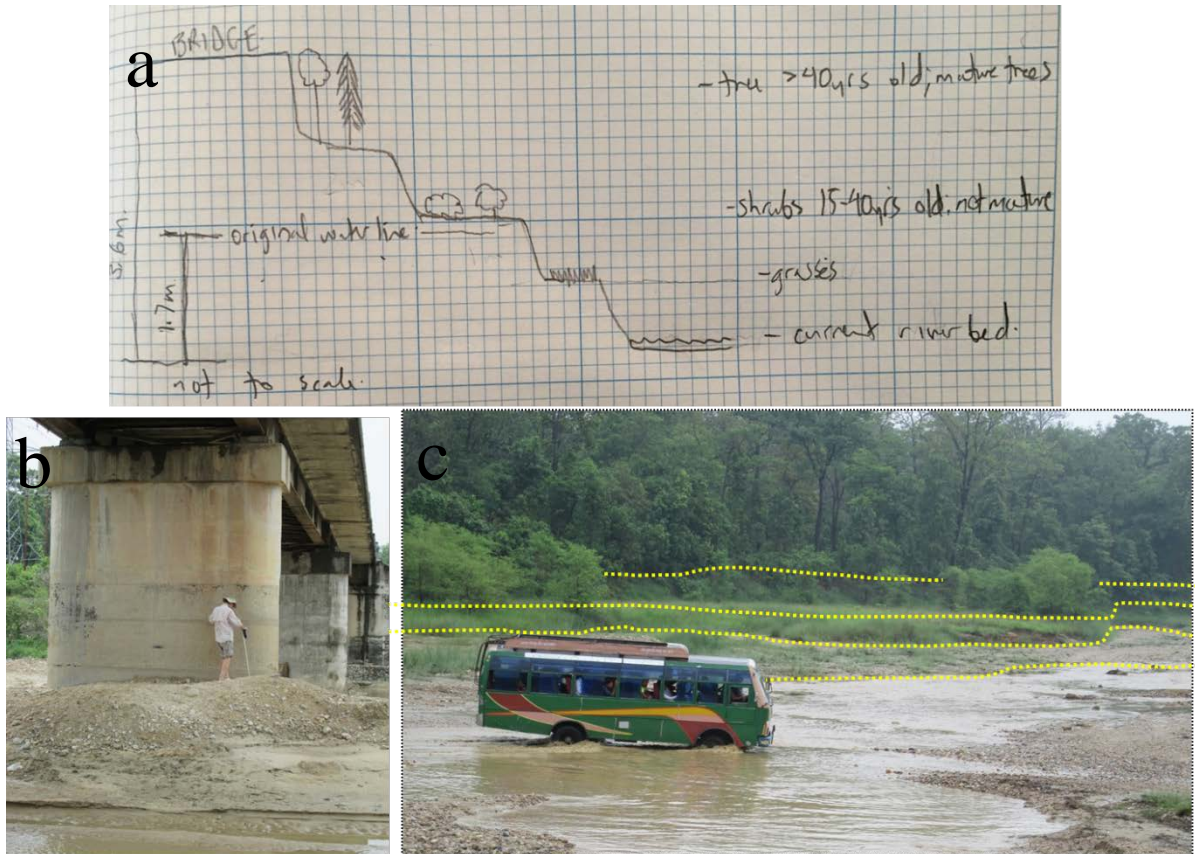
Figure 30. Various images of crossing at Dudhaura River: (a) cross section sketch of terraces from field notes, (b) current and original (at color change above head of person) river levels, and (c) annotated field photo of the terraces and vegetation adjacent to the river as shown in field sketch.

Attempts to alleviate the destruction of the Churia region are taking place. Figure 34

shows gabions installed where gravel excavation has taken place historically. The modern

riverbed can be seen in the background—likely causing destruction to the adjacent village

and farmland.

Figure 31. Gabions installed to help prevent additional erosion where gravel excavation has taken place.

5.2 LANDSLIDES AND TEMPORAL CHANGE

The results of the NDVI analysis showed that deforestation levels increased annually in the area of interest. This trend agrees with national deforestation statistics. The land use classifications showed that the woodlots have been cleared for agriculture and settlement. Additionally, as land was clear cut, landslides increased. The NDMIDIR outputs showed that very few landslides were large; most were small (many were only 450 m^2; the average size of the landslides in 2015 was 1455 m^2), yet these small landslides are undoubtedly locally destructive. Many of the landslides were likely reactivations of previous landslides, as the algorithm detected newer landslides on top of, or very close to, existing landslides. Figure 32 summarizes nearly 40 years of analysis of degradation of the Churia region. The graph shows that as NDVI levels decreased, urbanization, agriculture, and landslides increased. The landslide and flooding percentiles have been exaggerated for display purposes, by multipliers of 200 and 10, respectively. The flooding data is inconclusive.

58
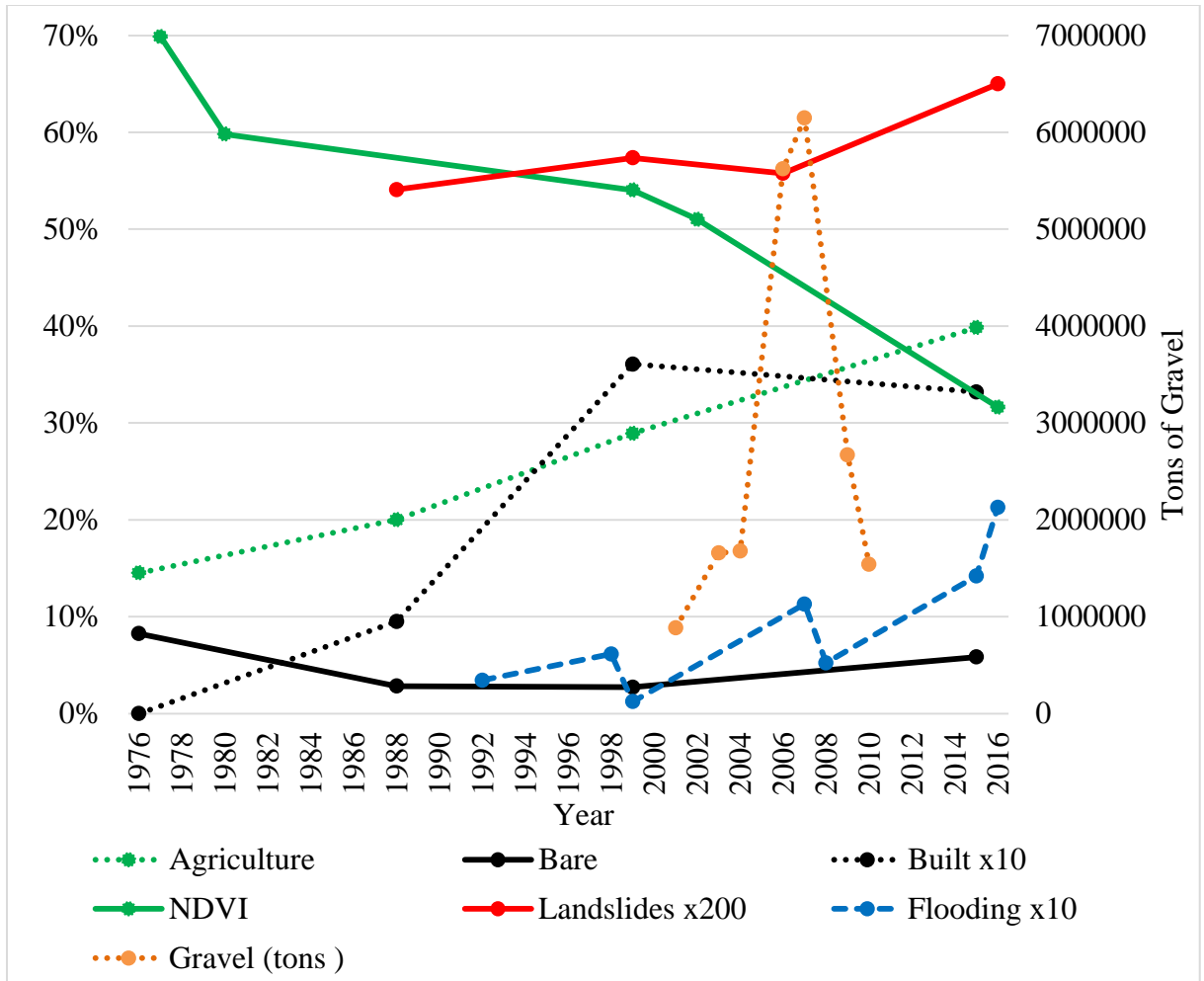
Figure 32. Degradation in Churia Region.

Researchers at Durham University and the British Geological Society conducted an image interpretation study to manually identify landslides after the 2015 earthquake. Figure 33 shows one of the manually identified landslides (yellow line) using Google Earth for display. The background image is a DigitalGlobe scene. Forest has been clear cut at the top and sides of the hill for settlement, agriculture, and likely logging. Scrub trees have begun to grow back in place of the logged forests but are not nearly as well rooted to keep the soil and slope in place as would forest cover. Agricultural land use is clearly visible at the base of the hill and undoubtedly was covered by the landslide material. Figure 34 shows the base of the

hill where the landslide debris settled. Also visible are smaller possible landslides to the right

of the identified landslide. A narrow road runs across the center of the landslide scar.

Figure 33. Example of manually identified landslide (yellow line) by the Durham University and the British Geological Society after the 2015 Nepal earthquake. DigitalGlobe image from Google Earth.

Figure 34. Base of landslide (yellow line) shown with homes and farmland impacted. Landslide manually identified by Durham University and the British Geological Society after the 2015 Nepal Earthquake. DigitalGlobe image from Google Earth.

Figure 35 compares the landslide identified by Durham University and the British

Geological Society (top) and this landslide detected by the modified NDMIDIR algorithm

applied to the 2015 Landsat image (bottom). A large landslide shown in Figure 35 on the left

was not detected manually by Durham University and the British Geological Society

researchers, perhaps because this landslide occurred after the British landslide study was

conducted or simply overlooked due to the risk of human error during manual image

interpretation. While the automated landslide detecting tool overestimates landslides, as

shown by the smaller "detected landslides," running an algorithm to detect landslides is more

efficient and removes the potential for human error during interpretation. The automated

landslide tool should be considered as a starting point for monitoring landslides to narrow

down in a specific area. After which, QA/QC and field work could omit overestimated

landslides.

Figure 35. Comparison of the landslide identified by Durham University and the British Geological Society (top) and this landslide detected by the modified NDMIDIR algorithm applied to the 2015 Landsat image (bottom). DigitalGlobe images from Google Earth.

5.3 RIVER FEATURES

Mapping temporal change of river inundation in the Terai and the extent to which river inundation exacerbates the Churia degradation process were inconclusive. Considering that the project planners had placed considerable emphasis on river inundation being to the determent of the Terai, the SAR data, even during peak monsoon conditions, showed very little, if any, river inundation associated with the Dudhaura River. Archived Google Earth imagery clearly shows that the Dudhaura River has at least three major manmade features crossing the river. Figure 36 shows one of these manmade features crossing the Dudhaura River with a 2009 DigitalGlobe imagery in the background. While the SAR data did not indicate substantial river inundation in the study area, the results do show significant flooding in North India. Undoubtedly, while these manmade structures are controlling/altering river flow as gravel has been excavated from the rivers of the study area, the riverbed has been dredged and widened, the gradient has become steeper, water velocities have increased and the flood plain widened. The rivers slow swiftly until they reach lower gradients in North India and flood there. The flooding has simply shifted further downstream.

Figure 36. Manmade feature built across the Dudhaura River shown in Google Earth. 2009 DigitalGlobe image in background.

5.4 GRAVEL

The gravel and sand data provided by the Nepal government included many different types of excavation materials recorded. However, instruction was given by the project planners to only include gravel smaller than 2 inches in size for this study as a test variable to see the trend on material export from the Birgunj Customs Office. Considering that the project planners had placed considerable emphasis on gravel excavation being to the determent of the Churia region, higher reported excavation quantities were expected. There might have been data entry errors by the customs office itself that cannot be resolved at this stage. The gravel data used for this study only represents one of the border crossings between Nepal and India. Additionally, the data does not consider excavated gravel that stayed within Nepal.

Overall, the general trend of the gravel data investigated showed that gravel excavation increased unrestricted through 2006 when the monarchy was abolished and there was massive disorder regarding the implementation of rules and regulations. Many of these gravel and sand excavators operated in the region illegally. The gravel trend line also shows that following this massive extraction of gravel from the Churia region and the subsequent outcry of the public and media, the government began attempts to place regulations on the gravel industry. These government interventions encouraged the decline in gravel exports shown between 2008-2010. In 2009 the Churia Conservation Program was initiated to create and monitor policy to preserve the Churia region and will undoubtedly play a role in further reducing illegal gravel excavation in the area (Pokhrel, 2013).

5.5 PRECIPITATION DATA

Like previous research focused on Nepal monsoons (Barros et al., 2000; Shrestha et al., 2000; Gillies et al., 2013; Devkota, 2014; Panthi et al., 2015) have shown, the average monthly precipitation data for Birgunj showed that landslides and flooding dangers in the Churia region stem from the simple fact that the region is in a constant state of suffering from either too much rain during monsoon seasons or not enough precipitation the rest of the year.

Simara Airport, Bara is 30 masl and Birgunj is 86 masl, while Hetauda, Makwanpur is 474 masl (Central Bureau of Statistics, 2013). The data show that Hetauda, Makwanpur receives more rain than Birgunj and almost always more rain than Simara. This is easily understood, as the winds carry moist air over the Terai plains (Simara and Birgunj) before the air reaches the Siwalik hills of Makwanpur, where the warm moist air encounters colder air from the Himalayas. The air cools as it rises over the mountains in its path, and since cool air cannot carry as much moisture as warm air, precipitation occurs. Hetauda in Makwanpur

district receives an additional 676 mm of rain on average each year compared to Simara in Bara district.

5.6 LANDSLIDE RISK MAP

Precipitation, geology, elevation, slope, aspect, lithology, land use, and the density of surface features, including roads, rivers, and settlement, all play a vital role in landslide risk potential. The Terai was not included in the final landslide risk map or risk calculations, as the elevations, slopes, and risk values were very low. The study area between the MFT and MBT have low to moderate risk of landslides, while the area north of the MBT almost entirely represented high to very high risk of landslides. South of the MBT has lower elevation and more gentle slopes, while elevations are higher and slopes steeper north of the MBT.

To validate the landslide risk map, the landslides manually interpreted in 2015 by Durham University and the British Geological Society were overlain on the landslide map. These manually identified landslides within the study area were in areas either deemed as very high (60%) or high (40%) landslide potential. The results of the weighted, multi-influencing, multi-variable modeling through GIS overlay analysis accurately mapped landslide risk potential in the area of interest. While the methods used in this study have not been tested in other districts of the Churia region of Nepal, the methods and model used to map landslide risk potential can be widely and efficiently applied as a valuable tool for understanding, predicting, and ultimately solving landslide risk potential elsewhere throughout the Churia region.

CHAPTER SIX: CONCLUSIONS

The people and infrastructure in the Churia region will continue to face serious and persistent geohazard threats so long as deforestation, agricultural mismanagement, and reckless exploitation of natural resources continue. The Churia Region is incredibly vulnerable to geohazards because of the young and fragile sandstone geology, gravel excavation, and forest conversion to agriculture and settlement. Remedies and mitigation measures for flooding, landslide, and deforestation issues in the region must include: ban or at least regulate illegal river bed gravel mining, initiate incentive programs to discourage the conversion of forest to farmland, initiate incentive programs to discourage farming on slopes, and continue to offer incentive programs regarding erosion control and land stabilization projects. Remedies and mitigation measures should also strengthen conservation incentives to manage forest resources, reinforce reforestation projects to rehabilitate degraded forests, rehabilitate degraded lands adjacent to the rivers for agricultural purposes, and identify alternative energy sources to alleviate the unsustainable pressure on the forests for fuel and building materials.

The optical imagery portion of this study demonstrates that temporal change of landslides in the Churia region is correlated with temporal changes in land use/deforestation/urbanization in the region. As forest cover has decreased over the last 40 years, urbanization, agriculture, and landslides have increased. The average rate of forest coverage loss is 1.03% per year. The SAR potion of this study was inconclusive in officially determining that river inundation in the Terai has exacerbated degradation in the Churia region. The gravel excavation measurements show that stone quarrying has exacerbated the Churia degradation process, but luckily, excavation is decreasing. Hetauda, Makwanpur

receives an additional 676 mm of rain on average each year compared to Simara in Bara. Based on these two precipitation stations, annual rainfall has been decreasing between 2001 and 2012.

A GIS model using weighted landslide variables derived from remote sensing and GIS methods successfully mapped landslide susceptibility. Nearly 70% of the Siwalik in the study area is at moderate to very high risk of landslides. The results of the GIS model can provide information for disaster managers and policy planners in landslide prone areas, not only in the Churia region of Nepal, but in other parts of the world vulnerable to landslides. Policy planners can use the model and output maps to guide their decisions regarding development in the areas that are at most risk for landslides and efficiently and economically decrease loss of lives and property in the region.

RECOMMENDATIONS

Future work should include visits to additional landslides to increase the sample size. The 30m spatial resolution of the imagery used was too low to distinguish types of mass movement based on spectral signature. Future work should include imagery available at higher spatial resolution (10m or smaller). Airphotos might help to define debris depositional zone to determine if the debris depositional zone is moving. Incorporating InSAR data would help to detect landslide activity.

REFERENCES

Abdullah, A., J. M. Akhir, and I. Abdullah, 2010, Automatic mapping of lineaments using shaded relief images derived from digital elevation model (DEMs) in the Maran-Sungi Lembing area, Malaysia, Electronic Journal of Geotechnical Engineering, v. 15, p. 949-957.

Abdullah, A, S. Nassr, and A. Ghaleeb, 2013, Remote Sensing and Geographic Information System for Fault Segments Mapping a Study from Taiz Area, Yemen: Journal of Geological Research, v. 2013, 1-16.

Akgun, A., C. Kıncal, and B. Pradhan, 2012, Application of remote sensing data and GIS for landslide risk assessment as an environmental threat to Izmir city (west Turkey): Environmental Monitoring and Assessment, v. 184 p. 5453-5470.

Al-doski, J., B. S. Mansor, and H. Z. M. Shafri, 2013, NDVI Differencing and postclassification to Detect Vegetation Changes in Halabja City, Iraq: IOSR Journal of Applied Geology and Geophysics, v. 1, no. 2, p. 1-10.

Argialas, D., O. Mavrantza, and M. Stefouli, 2003, Automatic mapping of tectonic lineaments (faults) using methods and techniques of photointerpretation/digital remote sensing and expert Systems: THALES Project, v. 1174, p. 1-6.

Awasthi, K. D., B. K. Sitaula, B. R. Singh, and R. M. Bajacharaya, 2002, Land-use change in two Nepalese watersheds: GIS and geomorphometric analysis: Land Degradation & Development, v. 13, no. 6, p. 495-513.

Badamasi, M. M., S. A. Yelwa, M.A. AbdulRahim, and S. S. Noma, 2012, NDVI threshold classification and change detection of vegetation cover at the Falgore Game Reserve in Kano State, Nigeria: Sokoto Journal of the Social Sciences, v. 2, no. 2, p. 174-194.

Bahadur, K. C., 2009, Improving Landsat and IRS image classification: evaluation of

    unsupervised and supervised classification through band ratios and DEM in a

    mountainous landscape in Nepal: Remote Sensing, v. 1, no. 4, p. 1257-1272.

Baidya, N. G., D. R. Bhuju, and P. Kandel, 2009, Land Use Change in Buffer Zone of

    Chitwan National Park, Nepal between 1978 and 1999: Ecoprint, An International

    Journal of Ecology, v. 16, p. 79-86.

Barlow, J., Y. Martin, and S. E. Franklin, 2003, Detecting translational landslide scars using

    segmentation of Landsat ETM+ and DEM data in the northern Cascade Mountains,

    British Columbia: Canadian journal of remote sensing, v. 29, no. 4, p. 510-517.

Barros, A. P., M. Joshi, J. Putkonen, and D. W. Burbank, 2000, A study of the 1999 monsoon

    rainfall in a mountainous region in central Nepal using TRMM products and rain

    gauge observations: Geophysical Research Letters, v. 27, no. 22, p. 3683-3686.

Baumgardner, R. W., and M. L. W. Jackson, 1987, LANDSAT-based lineament analysis,

    East Texas Basin, and structural history of the Sabine Uplift area, East Texas and

    North Louisiana: Texas Univ., Austin Report, v. 1, p. 1-26.

Baumgardener, R. W., 1991, Lineament analysis of northern San Juan Basin, New Mexico

    and Colorado-applications to coalbed methane exploration: Rocky Mountain

    Association of Geologists, Coalbed Methane of Western North America

Bhandari, N. B., R. Yatabe, R. K. Dahal, S. Hasegawa, and H. Inagaki, 2013, Areal

    distribution of large-scale landslides along highway corridors in central Nepal:

    Georisk, v. 7, p. 1–20.

Bhattarai, K., D. Conway, and M. Yousef, 2009, Determinants of deforestation in Nepal's central development region: Journal of Environmental Management, v. 91, no. 2, 471-488.

Bhattarai, B. C., and A. M. S. Pradhan, 2013, A Case Study on Landslide Hazard Mapping in Changunarayan VDC, Nepal: Landslide Science and Practice, Springer Berlin Heidelberg, p. 551-559.

Bhuju, D. R., P. B. Yonzon, and B. M. Baidya, 2007, Land use pattern and its change in the eastern Churiya hills of Nepal Himalaya: Ecoprint, v. 14, p. 65- 71.

Brewin, P. A., S. T. Buckton, and S. J. Ormerod, 2000, The seasonal dynamics and persistence of stream macroinvertebrates in Nepal: do monsoon floods represent disturbance?: Freshwater Biology, v. 44, no. 4, p. 581-594.

Cao, L., T. Liu, and L. Wei, 2014, A comparison of multi-resource remote sensing data for vegetation indices: Earth and Environmental Science, v.17 (1), p. 1-7.

Caran, C. S., C. M. Woodruff Jr, and E. J. Thompson, 1981, Lineament Analysis and Inference of Geologic Structure--Examples from the Balcones/Ouachita Trend of Texas (1): Gulf Coast Association of Geological Societies Transactions, v. 31, p. 59-63.

Central Bureau of Statistics, 2013, Environment Statistics of Nepal 2013, < http://cbs.gov.np/image/data/2015/Environment%20Statistics%20of%20Nepal%2020 13.pdf>, Accessed November 4, 2016.

Chaabouni, R., S. Bouaziz, H. Peresson, and J. Wolfgang, 2012, Lineament analysis of South Jenein Area (Southern Tunisia) using remote sensing data and geographic information system: The Egyptian Journal of Remote Sensing and Space Science, v. 15, no. 2, p. 197-206.

Chakraborty, R. N., 2001, Stability and outcomes of common property institutions in forestry: Evidence from the Terai region of Nepal: Ecological Economics, v. 36, no. 2, p. 341-353.

Copernicus, Sentinel, 2015 and 2016, Retrieved from ASF DAAC, 4 August 2016.

Dahal, R. K., and S. Hasegawa, T. Masuda, and M. Yamanaka, 2006, Roadside slope failures in Nepal during torrential rainfall and their mitigation. Disaster mitigation of debris flow, slope failures and landslides, Interpraevent 2007, Universal Academy Press, Tokyo, v. 2, p.503-514.

Dahal, R. K., and S. Hasegawa, 2008, Representative rainfall thresholds for landslides in the Nepal Himalaya: Geomorphology, v. 100, no. 3, p. 429-443.

Dahal, R. K., S. Hasegawa, A. Nonomura, M. Yamanaka, S. Dhakal, and P. Paudyal, 2008a, Predictive modelling of rainfall-induced landslide hazard in the Lesser Himalaya of Nepal based on weights-of-evidence, Geomorphology, v. 102, no. 3, p. 496-510.

Dahal, R. K., S. Hasegawa, A. Nonomura, M. Yamanaka, and S. Dhakal, 2008b, DEM-based deterministic landslide hazard analysis in the Lesser Himalaya of Nepal: Georisk, v. 2, no. 3, p. 161-178.

Dahal, R.K., S. Hasegawa, A. Nonomura, M. Yamanaka, T. Masuda, K. Nishino, 2008c, GIS-based weights-of-evidence modelling of rainfall-induced landslides in small catchments for landslide susceptibility mapping: Environmental Geology, v. 54, no. 2, p. 311-324.

Dahal, R. K., S. Hasegawa, M. Yamanaka, S. Dhakal, N. P. Bhandari, and R.Yatabe, 2009, Comparative analysis of contributing parameters for rainfall-triggered landslides in the Lesser Himalaya of Nepal: Environmental Geology, v. 58, no. 3, p. 567-586.

Dahal, R. K., S. Hasegawa, N. P. Bhandari, and R. Yatabe, 2010a, Low-cost road for the development of Nepal and its engineering geological consequences, In IAEG 2010 Conference, geologically active, Taylor & Francis Group, London, pp. 4085-4095.

Dahal, R. K., S. Hasegawa, M. Yamanaka, N. P. Bhandari, and R. Yatabe, 2010b, Statistical and deterministic landslide hazard assessment in the Himalayas of Nepal: IAEG 2010 conference, Geologically active, Taylor & Francis Group, London, p. 1053-1060.

Dahal, R. K., 2012, Rainfall-induced landslides in Nepal: International Journal of Erosion Control Engineering, v. 5, no. 1, p. 1-8.

Dahal, R. K., S. Hasegawa, N. P. Bhandari, P. P. Poudel, A. Nonomura, and R. Yatabe, 2012, A replication of landslide hazard mapping at catchment scale: Geomatics, Natural Hazards and Risk, v. 3 no. 2, p. 161-192.

Department of Mines and Geology, Government of Nepal, 2011, Geological Map of Central Nepal, Scale 1:250,000.

Devkota, K. C., A. D. Regmi, H. R. Pourghasemi, K. Y., B. Pradhan, I. C. Ryu, M. R. Dhital, and O. F. Althuwaynee, 2013, Landslide susceptibility mapping using certainty factor, index of entropy and logistic regression models in GIS and their comparison at Mugling–Narayanghat road section in Nepal Himalaya: Natural Hazards, v. 65, no. 1, p. 135-165.

Devkota, R.P., 2014, Climate change: trends and people's perception in Nepal: Journal of Environmental Protection, v. 5, no. 4, p. 255-265.

Drahovzal, J. A., 1974, Lineaments of northern Alabama and possible regional implications." Proceedings of the 1st International Confernce on the New Basement Tectonics, p. 250-261.

Durham University, 2016, Nepal 2015 Earthquakes: Landslide Updates <http://community.dur.ac.uk/nepal.2015eq/landslide-updates/> Accessed October 20, 2016.

Elmahdy, S. I., M. M. Marghany, and M. M. Mohamed, 2016, Application of a weighted spatial probability model in GIS to analyse landslides in Penang Island, Malaysia: Geomatics, Natural Hazards and Risk, v. 7, no. 1, p. 345-359.

ESRI, 2015, ArcGIS Desktop version 10.3.1.

European Space Agency, 2016a, eoPortal Directory: Satellite Missions Database, <https://directory.eoportal.org/web/eoportal/satellite-missions>, Accessed October 30, 2016.

European Space Agency, 2016b, Sentinels Application Platform version 4.0

Gautam, P., and E. Appel, 1994, Magnetic-polarity stratigraphy of Siwalik Group sediments of Tinau Khola section in west central Nepal, revisited: Geophysical Journal International, v. 117, no. 1, p. 223-234.

Gautam, P., A. Hosoi, K. R. Regmi, D. R. Khadka, and Y. Fujiwara, 2000, Magnetic minerals and magnetic properties of the Siwalik Group sediments of the Karnali river section in Nepal: Earth, planets and space, v. 52, no. 5, p. 337-345.

Gautam, A., G, Shivakoti and E. Webb, 2004, A review of forest policies, institutions, and changes in the resource condition in Nepal: International Forestry Review, v. 6, p. 136-148.

Ghimire, M., 2011, Landslide occurrence and its relation with terrain factors in the Siwalik Hills, Nepal Case study of susceptibility assessment in three basins: Natural Hazards, v. 56, p. 299-320.

Ghimire, S. K., D. Higaki, and T. P. Bhattarai, 2013, Estimation of soil erosion rates and eroded sediment in a degraded catchment of the Siwalik Hills, Nepal: Land, v. 2, no. 3, p. 370-391.

Gillies, R. R., S. Y. Wang, Y. Sun, and O. Y. Chung, 2013, Supportive empirical modelling for the forecast of monsoon precipitation in Nepal: International Journal of Climatology, v. 33, no. 14, p. 3047-3054.

Gokarn, S. G., C. K. Rao, and G. Gupta, 2002, Crustal structure in the Siwalik Himalayas using magnetotelluric studies:Earth, planets and space, v.54, no. 1, p. 19-30.

Government of Nepal National Planning Commission Secretariat Central Bureau of

    Statistics. 2012, National Population and Housing Census 2011,

    <http://cbs.gov.np/image/data/Population/VDC-

    Municipality%20in%20detail/VDC_Municipality.pdf>, Accessed October 30, 2016.

Hasegawa, S., R. K. Dahal, M. Yamanaka, N. P. Bhandari, R. Yatabe, and H. Inagaki, 2009a,

    Causes of large-scale landslides in the Lesser Himalaya of central Nepal:

    Environmental Geology, v. 57, p. 1423–1434

Hasegawa, S., R. K. Dahal, T. Nishimura, A. Nonomura, and M. Yamanaka, 2009b, DEM-

    Based Analysis of Earthquake-Induced Shallow Landslide Susceptibility:

    Geotechnical and Geological Engineering, v. 27, no. 3, p. 419-430.

Honda, K., L. Samarakoon, A. Ishibashi, Y. Mabuchi, and S. Miyajima, 1996, Remote

    sensing and GIS technologies for denudation estimation in a Siwalik watershed of

    Nepal: In Proceedings of of the 17th Asian Conference on Remote Sensing, Colombo,

    Sri Lanka, v 48, p. 1-26.

Jackson, R. D., and A. R. Huete, 1991, Interpreting vegetation indices: Preventive veterinary

    medicine, v. 11, no. 3, p. 185-200.

JAXA/METI ALOS PALSAR L1.0, 2007 and 2008, Accessed through ASF DAAC, 13 April

    2014.

JERS-1, JAXA, 1994, Retrieved from ASF DAAC, 27 March 2014.

Johnson, B., 2014, Effects of pansharpening on vegetation indices: ISPRS International

    Journal of Geo-Information, v. 3, no. 2, p. 507-522.

Kandel, C., 2009, Forest cover monitoring in the Bara district (Nepal) with remote sensing

    and geographic information systems, Doctoral dissertation.

Kayastha, P., M. R. Dhital, and F. De Smedt, 2013, Application of the analytical hierarchy process (AHP) for landslide susceptibility mapping: a case study from the Tinau watershed, west Nepal: Computers & Geosciences, v. 52, p. 398-408.

Kocal, A., H. S. Duzgun, and C. Karpuz, 2004, Discontinuity mapping with automatic lineament extraction from high resolution satellite imagery: ISPRS XX, Istanbul, p. 1-6.

Kowalik, W. S., and D. P. Gold, 1974, The use of Landsat-1 imagery in mapping lineaments in Pennsylvania: Procceedings of the 1st International Confernce on the New Basement Tectonics, p. 236-249.

Lane, S. N., R. M. Westaway, and D. M. Hicks, 2003, Estimation of erosion and deposition volumes in a large, gravel-bed, braided river using synoptic remote sensing: Earth Surface Processes and Landforms, v. 28, no. 3, p. 249-271.

Lee, S., and B. Pradhan, 2006, Probabilistic landslide hazards and risk mapping on Penang Island, Malaysia: Journal of Earth System Science, v. 115, no. 6, p. 661-672.

Lee, S., K. Song, H. Oh, and J. Choi, 2012, Detection of landslides using web-based aerial photographs and landslide susceptibility mapping using geospatial analysis: International Journal of Remote Sensing, v. 33, no. 16, p. 4937-4966.

Lillesand, T. M., R. W. Kiefer, and J. W. Chipman, 2015, Remote sensing and image interpretation, 7th Edition, John Wiley, New York, New York.

McCulloh, R. P., 2003, Lineaments and the Separation of Sicily Island from the Chalk Hills by the Ouachita River Valley, Northern Catahoula Parish, Louisiana: Louisiana Geological Survey News, v. 13, no. 1, p. 1-4.

Mallast, U., R. Gloaguen, S. Geyer, T. Rödiger, and C. Siebert, 2011a, Derivation of groundwater flow-paths based on semi-automatic extraction of lineaments from remote sensing data: Hydrology and Earth System Sciences, v. 15, no. 8 p. 2665-2678.

Mallast, U., R. Gloaguen, S. Geyer, T. Rödiger, and C. Siebert, 2011b, Semi-automatic extraction of lineaments from remote sensing data and the derivation of groundwater flow-paths: Hydrology Earth System Science Discuss, v. 8, p. 1399-1431.

Mancini, F., C. Ceppi, and G. Ritrovato, 2010, GIS and statistical analysis for landslide susceptibility mapping in the Daunia area, Italy: Natural Hazards and Earth System Science, v. 10, no. 9, p. 1851-1864.

Marghany, M., and M. Hashim, 2010, Lineament mapping using multispectral remote sensing satellite data: International Journal of Physical Sciences, v. 5, no. 10, p, 1501-1507

Metternicht, G., L. Hurni, and R. Gogu, 2005, Remote sensing of landslides: An analysis of the potential contribution to geo-spatial systems for hazard assessment in mountainous environments: Remote Sensing of Environment, v. 98, no2-3, p. 284-303.

Mugnier, J. L., P. Leturmy, G. Mascle, P. Huyghe, E. Chalaron, G. Vidal, L. Husson, and B. Delcaillau, 1999, The Siwaliks of western Nepal: I. Geometry and kinematics: Journal of Asian Earth Sciences, v. 17, no. 5, p. 629-642.

Muhammad, M. M., and A. H. Awdal, 2012, Automatic mapping of lineaments using shaded relief images derived from digital elevation model (DEM) in Erbil-Kurdistan, northeast Iraq: Advances in Natural and Applied Sciences, v. 6, no. 2, p. 138-147.

Mwaniki, M. W., N. O. Agutu, J. G. Mbaka, T. G. Ngigi, and E. H. Waithaka, 2015,

    Landslide Scar/Soil Erodibility Mapping Using Landsat TM/ETM+ Bands 7 And 3

    Normalized Difference Index: A Case Study of Central Region of Kenya: Applied

    Geography, v. 64, p. 108-120.

Nakayama, K. and P. D. Ulak, 1999, Evolution of fluvial style in the Siwalik Group in the

    foothills of the Nepal Himalaya: Sedimentary Geology, v. 125, p. 205-224.

NASA, 2016, Landsat Science, <http://landsat.gsfc.nasa.gov>, Accessed October 30, 2016.

Oh, H., N. Park, S. Lee, and S. Lee, 2012, Extraction of landslide-related factors from

    ASTER imagery and its application to landslide susceptibility mapping: International

    Journal of Remote Sensing, v. 33, no. 10, p. 3211-3231.

Pachauri, A. K., and M. Pant, 1992, Landslide hazard mapping based on geological

    attributes: Engineering geology, v. 32, no. 1-2, p. 81-100

Pachauri, A. K., P. V. Gupta, and R. Chander, 1998, Landslide zoning in a part of the

    Garhwal Himalayas: Environmental Geology, v. 36, no. 3-4, p. 325-334.

Pantanahiran, W., 2005, Using GIS and Remote Sensing to monitor the natural recovery of

    landslide areas in Thailand: Faculty of Social Science, Srinakharinwirot University, p.

    1-6.

Panthi, J., P. Dahal, M. L. Shrestha, S. Aryal, N. Y. Krakauer, S. M. Pradhanang, T.

    Lakhankar, A.K. Jha, M. Sharma, and R. Karki, 2015, Spatial and temporal

    variability of rainfall in the Gandaki River Basin of Nepal Himalaya: Climate, v.3,

    no. 1, p. 210-226.

Papadaki, E. S., S. P. Mertikas, and A. Sarris, 2011, Identification of lineaments with

possible structural origin using ASTER images and DEM derived products in

Western Crete, Greece: EARSeL eProceedings, v. 10, no. 1, p. 9-26

PCI Geomatics, 2015, Geomatica version 2015.

PCI Geomatics, 2016, Geomatica 2016 Users Guide.

<http://www.pcigeomatics.com/geomatica-help>, Accessed October 2, 2016.

Plummer, C.C., D. M. Geary, and D. H. Carlson, 2003, Physical Geology, 9th Ed.

McGraw Hill, New York.

Pokhrel, K. P., 2013, Chure forestry conservation and management plan: A case study of

Arghakhanchi district, Nepal: Journal of Geography and Regional Planning, v. 6, no.

5, p. 172-183.

Poudyal, C. P., 2013, Landslide susceptibility analysis using decision tree method, Phidim,

Eastern Nepal: Bulletin of the Department of Geology, v. 15, p. 69-76.

Pradhan, B., R. P. Singh, and M. F. Buchroithner, 2006, Estimation of stress and its use in

evaluation of landslide prone regions using remote sensing data: Advances in Space

Research, v. 37, no. 4, p. 698-709.

Pradhan B, S. Mansor, S. Lee, M. F. Buchroithner, 2008, Application of data mining model

for landslide hazard mapping, In Proceedings of ISPRS, v. 37, no. 8, p. 187-196.

Pradhan, B., S. Lee, and M. F. Buchroithner, 2009, Use of geospatial data and fuzzy

algebraic operators to landslide-hazard mapping: Applied Geomatics, v. 1 p. 3-15.

Pradhan, B., 2010, Flood susceptible mapping and risk area delineation using logistic

regression, GIS and remote sensing: Journal of Spatial Hydrology, v. 9, no. 2, p. 1-18.

Qari, M. H, 2011, Lineament extraction from multi-resolution satellite imagery: a pilot study on Wadi Bani Malik, Jeddah, Kingdom of Saudi Arabia: Arabian Journal of Geosciences, v. 4, no. 7-8, p. 1363-1371.

RADARSAT-1, CSA, 2014, Retrieved from ASF DAAC, 27 March 2014.

Rahnama, M. and R. Gloaguen. 2014, Teclines: A matlab-based toolbox for tectonic lineament analysis from satellite images and dems, part 2: Line segments linking and merging: Remote Sensing, v. 6, p. 11468-11493.

Ramli, M. F., N. K. Tripathi, N. Yusof, H. Z. M. Shafri, and Z. A. Rahman, 2009, Lineament Mapping in a Tropical Environment using Landsat Imagery: International Journal of Remote Sensing, v. 30, no. 23, p. 6277 – 6300.

Rastrapati Chure Conservation Program, data unknown, Welcome Rastrapati Chure Conservation Program Coordination Unit, <http://rccp.gov.np>, Accessed October 30, 2016.

Raut, S., and D. Panthi, 2015, Crushing tale of the Chure: Nepal Times, <http://nepalitimes.com/page/crushing-tale-of-Chure>, Accessed October 30, 2016.

Ray, R. L., and F. De Smedt, 2009, Slope stability analysis on a regional scale using GIS: a case study from Dhading, Nepal: Environmental geology, v. 57, no. 7, p. 1603-1611.

Rodgers, M. R., and T. H. Anderson, 1984, Tyrone-Mt. Union cross-strike lineament of Pennsylvania: A major Paleozoic basement fracture and uplift boundary: AAPG Bulletin, v. 68, no. 1, p. 92-105.

Sarkar S, D. P, Kanungo, A. K. Patra, P. Kumar, 2006, GIS Based landslide susceptibility mapping- case study in Indian Himalaya: Disaster mitigation of debris flows, slope failures and landslides, p. 617-624.

Schelling, D., J. Cater, R. Seago, and T. P. Ojha, 1991, A balanced cross-section across the
       Central Nepal Siwalik Hills; Hitauda to Amlekhganj: Journal of the Faculty of
       Science, Hokkaido University, series 4, Geology and mineralogy, v. 23, no. 1, p. 1-9.

Shanker, D., H. Paudyal, and H. N. Singh, 2011, Discourse on seismotectonics of Nepal
       Himalaya and vicinity: appraisal to earthquake hazard: Geosciences, v. 1, no. 1, p. 1-
       15.

Shrestha, A. B., C. P. Wake, J. E. Dibb, and P. A. Mayewski, 2000, Precipitation fluctuations
       in the Nepal Himalaya and its vicinity and relationship with some large scale
       climatological parameters: International Journal of Climatology, v. 20, no. 3, p. 317-
       327.

Shrestha, M. S., N. K. Tamrakar, and T. Miyazaki, 2009, Morphometry and sediment
       dynamics of the Churiya River area, Siwalik Range in Nepal: Boletin de geologia, v.
       30, no. 2, p. 35-48.

Shurr, G. W., 1982, Geological significance of lineaments interpreted from Landsat images
       near the northern Black Hills: Williston Basin Symposium, 1982. 4th International
       Williston Basin Symposium.

Sigdel, A., T. Sakai, P. D. Ulak, A. P. Gajurel, and B. N. Upreti: 2011, Lithostratigraphy of
       the Siwalik Group, Karnali River section, far-west Nepal Himalaya: Journal of Nepal
       Geological Society, v. 43, p. 83-101.

Singh, L.G., A.K. Naithani, D.S. Rawat and P.C. Nawani, 2013, Geological, lineament and
       landslide studies of the reservoir and its vicinity of Bunakha hydroelectric project,
       Bhutan Himalaya: Journal of Engineering Geology, v. 38, no. 1, p. 90-111.

Subedi, D. N., S. P. Mahato, S.B. KC, and J. R. Ghimire, 2012, Oil and gas Exploration

    Activities in Nepal: ASEG Extended Abstracts, v. 1, p. 1-4.

Sudmeier, K. I., M. Jaboyedoff, and S. Jaquet, 2013, Operationalizing "resilience" for

    disaster risk reduction in mountainous Nepal: Disaster Prevention and

    Management, v. 22, no. 4, p. 366-377

Süzen, M. L., and V. Doyuran, 2004. A comparison of the GIS based landslide susceptibility

    assessment methods: Multivariate versus bivariate: Environmental Geology, v. 45,

    no. 5, p. 665-679.

Syangbo, D. K., & N. K. Tamrakar, 2013, Lithofacies and depositional environment of the

    Siwalik Group in Samari-Sukaura River area, Central Nepal.Bulletin of the

    Department of Geology, v. 16, 53-64.

Syvitski, J. P. M., and G. R. Brakenridge, 2013, Causation and avoidance of catastrophic

    flooding along the Indus River, Pakistan: GSA Today, v. 23, v. 1, p. 4-10.

Tamrakar, N. K., & D. Khakurel, 2012, Lithologic and morphometric characteristics of the

    Chure River Basin, Central Nepal: Bulletin of the Department of Geology, v. 15, p.

    35-48.

Tamrakar, N. K. and D. K. Syangbo, 2014, Petrography and provenance of the Siwalik

    Group sandstones from the Main Boundary Thrust region, Samari river area, Central

    Nepal, sub-Himalaya: Boletín de Geología, v. 36, no. 2, p. 25-44.

Tembe, D., 2001, Community Forestry and Integrated Natural Resource Management in the

    Churia Region of Nepal: Journal of Forestry and Livelihoods, v. 1, no. 1, p. 9-11

Thannoun, R. G., 2013, Automatic extraction and geospatial analysis of lineaments and their tectonic significance in some areas of Northern Iraq using remote sensing techniques and GIS: International Journal of Enhanced Research In Science Technology & Engineering Bulletin, v. 2, no. 2, p. 1-11.

Tiwari, B., and R. Douglas, 2012, Application of GIS tools for three-dimensional slope stability analysis of pre-existing landslides: GeoCongress 2012: State of the Art and Practice in Geotechnical Engineering ASCE, p. 1-10.

Travaglia, C., and N. Dainelli, 2003, Groundwater search by remote sensing: A methodological approach: Environment and Natural Resources Working Paper, FAO, Rome, v. 13, p. 1-41.

Uddin, K, and B. Shrestha, 2011, Assessing flood and flood damage using Remote Sensing: a case study from Sunsari, Nepal: 3rd International Conference on Water and Flood Management, p. 293-301.

Upreti, B., 1999, An overview of the stratigraphy and tectonics of the Nepal Himalaya: Journal of Asian Earth Sciences, v. 17, no. 5-6, p. 577-606.

Upreti, B. N., 2001, The physiography and geology of Nepal and their bearing on the landslide problem: Landslide Hazard Mitigation in the Hindu Kush-Himalayas, p. 31-49.

Van Westen, C. J., T. W. J. Van Asch, and R. Soeters, 2006, Landslide hazard and risk zonation—why is it still so difficult?: Bulletin of Engineering geology and the Environment, v. 65, no. 2, p. 167-184

Veci, L., 2016, Sentinel-1 Toolbox SAR Basics Tutorial.
<http://sentinel1.s3.amazonaws.com/docs/S1TBX%20SAR%20Basics%20Tutorial.p
df>, Accessed August 2016.

Vohora, V. K., and S. L. Donoghue, 2004, Application of remote Sensing data to Landslide
mapping in Hong Kong: International Archives of Photogrammetry, Remote Sensing
and Spatial Information Sciences, v. 35, p. 489–494.

Weirich, F., and L. Blesius, 2007, Comparison of satellite and air photo based landslide
susceptibility maps: Geomorphology, v. 87, no. 4, p. 352-364.

Xu, L., S. Zhang, Z. He, and Y. Guo, 2009, The comparative study of three methods of
remote sensing image change detection, IEEE 17th International Conference on
Geoinformatics, p. 1-4.

Yengoh, G. T., D. Dent, L. Olsson, A. E. Tengberg and C. J. Tucker, 2014, The use of the
Normalized Difference Vegetation Index (NDVI) to assess land degradation at
multiple scales: a review of the current status, future trends, and practical
considerations. Lund University Center for Sustainability Studies (LUCSUS), and
The Scientific and Technical Advisory Panel of the Global Environment Facility
(STAP/GEF).

Yin, A., 2006, Cenozoic tectonic evolution of the Himalayan orogen as constrained by along-
strike variation of structural geometry, exhumation history, and foreland
sedimentation: Earth-Science Reviews, v. 76, no. 1, p. 1-131.

Zhang, S. and Xu, L., 2008, The Comparative study of three methods of remote sensing
image change detection: The International Archives of the Photogrammetry, Remote
Sensing and Spatial Information Services, v. 37, p. 1595–1598.

APPENDIX A: RASTER, VECTOR, AND TABULAR DATA USED

Layer	Data Type	Source	Source Website
ASTER Global DEM	raster	NASA	http://asterweb.jpl.nasa.gov/gdem.asp
Aspect	raster	Derived from DEM	
Slope	raster	Derived from DEM	
Districts	polygon	Ministry of Federal Affairs and Local Development (MoFALD)	https://data.humdata.org/dataset/admin-shapefiles-of-nepal-mofald
Field work GPS points	points		NA
Geology Map of Central Nepal	polygon	digitized based jpg published Department of Mines and Geology, Kathmandu, 2011	http://gis.dmgnepal.gov.np/dmg/
Thrusts and Faults	polyline	digitized based on Geological Map of Central Nepal and several journal article maps	
Gravel and sand export at Birgunj, Nepal border crossing	tabular	Department of Customs, Central office, Kathmandu, Nepal	
Landslides	lines	Durham University and British Geological Survey	https://data.humdata.org/dataset/nepal-earthquake-landslide-locations-30-june-2015
Nepal Total Annual Rainfall Distribution	raster	United Nations	https://data.humdata.org/dataset/nepal-historical-annual-and-monthly-rainfall-distribution-for-monsoon-months
Landsat 2 MSS	raster	United States Geological Survey	http://earthexplorer.usgs.gov/
Landsat 5 TM	raster	United States Geological Survey	http://earthexplorer.usgs.gov/
Landsat 7 ETM+	raster	United States Geological Survey	http://earthexplorer.usgs.gov/
Landsat OLI	raster	United States Geological Survey	http://earthexplorer.usgs.gov/
Physiography	polygon	ICIMOD	http://geoportal.icimod.org/Home/DataSets
RADARSAT-1 SAR ST4	raster	Canadian Space Agency	https://vertex.daac.asf.alaska.edu/
JERS-1 SAR	raster	Japan Aerospace Exploration Agency (JAXA).	https://vertex.daac.asf.alaska.edu/

Layer	Data Type	Source	Source Website
PALSAR FBS	raster	Japan Aerospace Exploration Agency (JAXA).	https://vertex.daac.asf.alaska.edu/
Sentinel 1A IWS	raster	European Space Agency	https://vertex.daac.asf.alaska.edu/
Rivers	polygon and polyline	Survey Department, Nepal	https://data.humdata.org/dataset/248e54c6-f113-4bd3-8083-a5d4a9eb5f79
Roads	polyline	Survey Department, Nepal	www.geofabrik.de
Settlements	points	ICIMOD	http://geoportal.icimod.org/Home/DataSets
World Political Boundaries	polygon	ESRI	https://www.arcgis.com/home/item.html?id=3864c63872d84aec91933618e3815dd2
Lithology	polygon	ISRIC.org	http://www.isric.org/content/download-form?dataset=SOTER_NP.zip
Normalized Difference Vegetation Index (NDVI)	polygon	Derived from Landsat imagery	
Landslides	polygon	Derived from Landsat imagery, DEM, and land use classification	
Lineaments	polygon	Derived from Landsat imagery	

APPENDIX B: PYTHON SCRIPT FOR WEIGHTED SUM LANDSLIDE RISK MAP

```
# -*- coding: utf-8 -*-
# ---------------------------------------------------------------------------
# risk_map.py
# Created on: 2016-11-29 07:43:12.00000
#   (generated by ArcGIS/ModelBuilder)
# Description:
# ---------------------------------------------------------------------------

# Import arcpy module
import arcpy


# Local variables:
GEOLOGY = "npl_polbnda_adm3_dis_MoFALD_HRRP_DISSOLVED_GEOLOGY"
Geology_Project =
"G:\\THESIS\\RISK_MAP\\inputs\\Landslide_risk.gdb\\Geology_Project"
Geology__3_ = "G:\\THESIS\\RISK_MAP\\inputs\\Landslide_risk.gdb\\Geology"
Reclass_Geology =
"G:\\THESIS\\RISK_MAP\\inputs\\Landslide_risk.gdb\\Reclass_Geology"
v2015_CLF = "G:\\THESIS\\RISK_MAP\\inputs\\2015-10-
07_LC81410412015280LGN00_atcore_CLIPPED_merged.tif"
Reclass_Classification =
"G:\\THESIS\\RISK_MAP\\inputs\\Landslide_risk.gdb\\Reclass_Classification"
WATER_line = "G:\\THESIS\\GIS\\River\\Riverdd.shp"
AOI =
"G:\\THESIS\\GIS\\District\\npl_polbnda_adm3_dis_MoFALD_HRRP_DISSOLVED.shp"
Water_Clip = "G:\\THESIS\\RISK_MAP\\inputs\\Landslide_risk.gdb\\Water_Clip"
Water_Project = "G:\\THESIS\\RISK_MAP\\inputs\\Landslide_risk.gdb\\Water_Project"
Water_density = "G:\\THESIS\\RISK_MAP\\inputs\\Landslide_risk.gdb\\Water_density"
Reclass_Water_density =
"G:\\THESIS\\RISK_MAP\\inputs\\Landslide_risk.gdb\\Reclass_Water_density"
Lithology = "NEPAL_SOTER"
Lithology_clip = "G:\\THESIS\\RISK_MAP\\inputs\\Landslide_risk.gdb\\Lithology_clip"
Lithology_Project =
"G:\\THESIS\\RISK_MAP\\inputs\\Landslide_risk.gdb\\Lithology_Project"
Lithology__2_ = "G:\\THESIS\\RISK_MAP\\inputs\\Landslide_risk.gdb\\Lithology"
Reclass_Lithology =
"G:\\THESIS\\RISK_MAP\\inputs\\Landslide_risk.gdb\\Reclass_Lithology"
roads = "roads_UTM"
Roads_Clip = "G:\\THESIS\\RISK_MAP\\inputs\\Landslide_risk.gdb\\Roads_Clip"
Roads_Project = "G:\\THESIS\\RISK_MAP\\inputs\\Landslide_risk.gdb\\Roads_Project"
Roads_Buffer =
"G:\\THESIS\\RISK_MAP\\inputs\\Landslide_risk.gdb\\Roads_MultipleRingBuffer"
Roads__2_ = "G:\\THESIS\\RISK_MAP\\inputs\\Landslide_risk.gdb\\Roads"
```

Reclass_Road_buffered =
"G:\\THESIS\\RISK_MAP\\inputs\\Landslide_risk.gdb\\Reclass_Road_buffered"
Road_Density = "G:\\THESIS\\RISK_MAP\\inputs\\Landslide_risk.gdb\\Road_Density"
Reclass_Road = "G:\\THESIS\\RISK_MAP\\inputs\\Landslide_risk.gdb\\Reclass_Road"
Precip_tif = "Precip_UTM.tif"
Precip_clip = "G:\\THESIS\\RISK_MAP\\inputs\\Landslide_risk.gdb\\Precip_clip"
Precip_Project = "G:\\THESIS\\RISK_MAP\\inputs\\Landslide_risk.gdb\\Precip_Project"
Precip_Resample =
"G:\\THESIS\\RISK_MAP\\inputs\\Landslide_risk.gdb\\Precip_Resample"
Reclass_Precipitation =
"G:\\THESIS\\RISK_MAP\\inputs\\Landslide_risk.gdb\\Reclass_Precipitation"
NDVI = "NDVI_2016-05-18_LC81410412016139LGN00_atcore.tif"
NDVI_Clip = "G:\\THESIS\\RISK_MAP\\inputs\\Landslide_risk.gdb\\NDVI_Clip"
Reclass_NDVI = "G:\\THESIS\\RISK_MAP\\inputs\\Landslide_risk.gdb\\Reclass_NDVI"
DEM_tif = "DEM.tif"
DEM_Clip = "G:\\THESIS\\RISK_MAP\\inputs\\Landslide_risk.gdb\\DEM_Clip"
DEM_Project = "G:\\THESIS\\RISK_MAP\\inputs\\Landslide_risk.gdb\\DEM_Project"
DEM_Resample = "G:\\THESIS\\RISK_MAP\\inputs\\Landslide_risk.gdb\\DEM_Resample"
Reclass_DEM = "G:\\THESIS\\RISK_MAP\\inputs\\Landslide_risk.gdb\\Reclass_DEM"
Aspect__2_ = "G:\\THESIS\\RISK_MAP\\inputs\\Landslide_risk.gdb\\Aspect"
Aspect_Resample =
"G:\\THESIS\\RISK_MAP\\inputs\\Landslide_risk.gdb\\Aspect_Resample"
Reclass_Aspect = "G:\\THESIS\\RISK_MAP\\inputs\\Landslide_risk.gdb\\Reclass_Aspect"
Slope__2_ = "G:\\THESIS\\RISK_MAP\\inputs\\Landslide_risk.gdb\\Slope"
Slope_Resample = "C:\\Users\\Amit\\Documents\\ArcGIS\\Default.gdb\\Slope_Resample"
Reclass_Slope = "G:\\THESIS\\RISK_MAP\\inputs\\Landslide_risk.gdb\\Reclass_Slope"
Thrusts___Faults = "Thrusts"
Thrusts_Clip = "G:\\THESIS\\RISK_MAP\\inputs\\Landslide_risk.gdb\\Thrusts_Clip"
Thrusts_Project = "G:\\THESIS\\RISK_MAP\\inputs\\Landslide_risk.gdb\\Thrusts_Project"
Thrusts_buffer =
"G:\\THESIS\\RISK_MAP\\inputs\\Landslide_risk.gdb\\Thrusts_Multi_buffer"
Thrusts__2_ = "G:\\THESIS\\RISK_MAP\\inputs\\Landslide_risk.gdb\\Thrusts"
Reclass_Thrusts = "G:\\THESIS\\RISK_MAP\\inputs\\Landslide_risk.gdb\\Reclass_Thrusts"
Settlement = "Settlementsdd"
Settlement_Clip = "G:\\THESIS\\RISK_MAP\\inputs\\Landslide_risk.gdb\\Settlement_Clip"
Settlement_Project =
"G:\\THESIS\\RISK_MAP\\inputs\\Landslide_risk.gdb\\Settlement_Project"
Settlement_buffer =
"G:\\THESIS\\RISK_MAP\\inputs\\Landslide_risk.gdb\\Settlement_buffer"
Settlement__2_ = "G:\\THESIS\\RISK_MAP\\inputs\\Landslide_risk.gdb\\Settlement"
Reclass_Settlement =
"G:\\THESIS\\RISK_MAP\\inputs\\Landslide_risk.gdb\\Reclass_Settlement"
WATER_poly = "npl_watcrsa_hydro_25K_50K_sdn_wgs84_dissolved"
WaterPoly_Clip = "G:\\THESIS\\RISK_MAP\\inputs\\Landslide_risk.gdb\\WaterPoly_Clip"
WaterPoly_Project =
"G:\\THESIS\\RISK_MAP\\inputs\\Landslide_risk.gdb\\WaterPoly_Project"

```
WaterPoly_Buffer =
"G:\\THESIS\\RISK_MAP\\inputs\\Landslide_risk.gdb\\WaterPoly_MultipleRingBuffer"
Water = "G:\\THESIS\\RISK_MAP\\inputs\\Landslide_risk.gdb\\Water"
Reclass_Water = "G:\\THESIS\\RISK_MAP\\inputs\\Landslide_risk.gdb\\Reclass_Water"
LANDSLIDES = "2015_NDMIDIR_LANDSLIDES"
Landslides_clip = "G:\\THESIS\\RISK_MAP\\inputs\\Landslide_risk.gdb\\Landslides_clip"
Landslides_buffer =
"G:\\THESIS\\RISK_MAP\\inputs\\Landslide_risk.gdb\\Landslides_buffer"
Landslides__2_ = "G:\\THESIS\\RISK_MAP\\inputs\\Landslide_risk.gdb\\Landslides"
Reclass_Landslides =
"G:\\THESIS\\RISK_MAP\\inputs\\Landslide_risk.gdb\\Reclass_Landslides"
LINEAMENTS = "G:\\THESIS\\imagery\\Landsat\\1_lineaments\\2015-12-
26_LC81410412015360LGN00_atcore_LINEAMENT.shp"
Lineaments_buffer =
"G:\\THESIS\\RISK_MAP\\inputs\\Landslide_risk.gdb\\Lineaments_buffer"
Lineaments__2_ = "G:\\THESIS\\RISK_MAP\\inputs\\Landslide_risk.gdb\\Lineaments"
Reclass_Lineaments =
"G:\\THESIS\\RISK_MAP\\inputs\\Landslide_risk.gdb\\Reclass_Lineaments"
Landslide_risk = "G:\\THESIS\\RISK_MAP\\inputs\\Landslide_risk.gdb\\Weighted_Sum"
Terai_clipper_shp = "G:\\THESIS\\trash\\Terai_clipper.shp"
Landslide_risk_clip =
"G:\\THESIS\\RISK_MAP\\inputs\\Landslide_risk.gdb\\Weighted_Sum_clipped"
Reclass_landslide_risk_clip =
"G:\\THESIS\\RISK_MAP\\inputs\\Landslide_risk.gdb\\Reclass_Weighted_sum"
landslide_raster2poly =
"G:\\THESIS\\RISK_MAP\\inputs\\Landslide_risk.gdb\\ReclassWeightedSum_raster2poly"
landslide_risk_shp =
"G:\\THESIS\\RISK_MAP\\inputs\\Landslide_risk.gdb\\ReclassWeightedSum_raster2poly_d
issolved"

# Set Geoprocessing environments
arcpy.env.snapRaster = "G:\\THESIS\\RISK_MAP\\inputs\\aoi_raster"
arcpy.env.extent = "269148.591670982 2959320.64366214 352458.591670982
3066810.64366214"
arcpy.env.mask = "G:\\THESIS\\RISK_MAP\\inputs\\aoi_raster"

# Process: Project (6)
arcpy.Project_management(GEOLOGY, Geology_Project,
"PROJCS['WGS_1984_UTM_Zone_45N',GEOGCS['GCS_WGS_1984',DATUM['D_WGS_
1984',SPHEROID['WGS_1984',6378137.0,298.257223563]],PRIMEM['Greenwich',0.0],UN
IT['Degree',0.0174532925199433]],PROJECTION['Transverse_Mercator'],PARAMETER['F
alse_Easting',500000.0],PARAMETER['False_Northing',0.0],PARAMETER['Central_Merid
ian',87.0],PARAMETER['Scale_Factor',0.9996],PARAMETER['Latitude_Of_Origin',0.0],U
NIT['Meter',1.0]]", "",
"GEOGCS['GCS_WGS_1984',DATUM['D_WGS_1984',SPHEROID['WGS_1984',6378137.
```

0,298.257223563]],PRIMEM['Greenwich',0.0],UNIT['Degree',0.0174532925199433]]",
"NO_PRESERVE_SHAPE", "")

Process: Polygon to Raster (3)
arcpy.PolygonToRaster_conversion(Geology_Project, "Geology", Geology__3_,
"CELL_CENTER", "NONE", "30")

Process: Reclassify (14)
arcpy.gp.Reclassify_sa(Geology__3_, "Geology", "Pre-Cambrian 10;Recent 0;'Lower
Siwalik' 1;'Upper Middle Siwalik' 8;'Lower Middle Siwalik' 2;'Upper Siwalik' 8;'Middle
Mountain' 10", Reclass_Geology, "DATA")

Process: Reclassify (8)
arcpy.gp.Reclassify_sa(v2015_CLF, "Value", "0 NODATA;1 3;2 8;3 10;4 5;5 1;6 1",
Reclass_Classification, "DATA")

# Process: Clip (5)
arcpy.Clip_analysis(WATER_line, AOI, Water_Clip, "")

Process: Project (4)
arcpy.Project_management(Water_Clip, Water_Project,
"PROJCS['WGS_1984_UTM_Zone_45N',GEOGCS['GCS_WGS_1984',DATUM['D_WGS_
1984',SPHEROID['WGS_1984',6378137.0,298.257223563]],PRIMEM['Greenwich',0.0],UN
IT['Degree',0.0174532925199433]],PROJECTION['Transverse_Mercator'],PARAMETER['F
alse_Easting',500000.0],PARAMETER['False_Northing',0.0],PARAMETER['Central_Merid
ian',87.0],PARAMETER['Scale_Factor',0.9996],PARAMETER['Latitude_Of_Origin',0.0],U
NIT['Meter',1.0]]", "",
"GEOGCS['GCS_WGS_1984',DATUM['D_WGS_1984',SPHEROID['WGS_1984',6378137.
0,298.257223563]],PRIMEM['Greenwich',0.0],UNIT['Degree',0.0174532925199433]]",
"NO_PRESERVE_SHAPE", "")

Process: Line Density (3)
arcpy.gp.LineDensity_sa(Water_Project, "NONE", Water_density, "30",
"2767.53116333333", "SQUARE_KILOMETERS")

Process: Reclassify
arcpy.gp.Reclassify_sa(Water_density, "Value", "0 0.10884892940521237
1;0.10884892940521237 0.30093527541441056 2;0.30093527541441056
0.48661874322330212 3;0.48661874322330212 0.78755401863771257
9;0.78755401863771257 1.632733941078186 10", Reclass_Water_density, "DATA")

# Process: Clip (2)
arcpy.Clip_analysis(Lithology, AOI, Lithology_clip, "")

Process: Project (2)

```
arcpy.Project_management(Lithology_clip, Lithology_Project,
"PROJCS['WGS_1984_UTM_Zone_45N',GEOGCS['GCS_WGS_1984',DATUM['D_WGS_
1984',SPHEROID['WGS_1984',6378137.0,298.257223563]],PRIMEM['Greenwich',0.0],UN
IT['Degree',0.0174532925199433]],PROJECTION['Transverse_Mercator'],PARAMETER['F
alse_Easting',500000.0],PARAMETER['False_Northing',0.0],PARAMETER['Central_Merid
ian',87.0],PARAMETER['Scale_Factor',0.9996],PARAMETER['Latitude_Of_Origin',0.0],U
NIT['Meter',1.0]]", "",
"GEOGCS['GCS_WGS_1984',DATUM['D_WGS_1984',SPHEROID['WGS_1984',6378137.
0,298.257223563]],PRIMEM['Greenwich',0.0],UNIT['Degree',0.0174532925199433]]",
"NO_PRESERVE_SHAPE", "")

# Process: Polygon to Raster (6)
arcpy.PolygonToRaster_conversion(Lithology_Project, "Parent_Mat", Lithology__2_,
"CELL_CENTER", "NONE", "30")

# Process: Reclassify (11)
arcpy.gp.Reclassify_sa(Lithology__2_, "Value", "1 10;2 8;3 1;4 7;5 9;6 6;7 6;8 0",
Reclass_Lithology, "DATA")

# Process: Clip (6)
arcpy.Clip_analysis(roads, AOI, Roads_Clip, "")

# Process: Project (5)
arcpy.Project_management(Roads_Clip, Roads_Project,
"PROJCS['WGS_1984_UTM_Zone_45N',GEOGCS['GCS_WGS_1984',DATUM['D_WGS_
1984',SPHEROID['WGS_1984',6378137.0,298.257223563]],PRIMEM['Greenwich',0.0],UN
IT['Degree',0.0174532925199433]],PROJECTION['Transverse_Mercator'],PARAMETER['F
alse_Easting',500000.0],PARAMETER['False_Northing',0.0],PARAMETER['Central_Merid
ian',87.0],PARAMETER['Scale_Factor',0.9996],PARAMETER['Latitude_Of_Origin',0.0],U
NIT['Meter',1.0]]", "",
"PROJCS['WGS_1984_UTM_Zone_45N',GEOGCS['GCS_WGS_1984',DATUM['D_WGS_
1984',SPHEROID['WGS_1984',6378137.0,298.257223563]],PRIMEM['Greenwich',0.0],UN
IT['Degree',0.0174532925199433]],PROJECTION['Transverse_Mercator'],PARAMETER['F
alse_Easting',500000.0],PARAMETER['False_Northing',0.0],PARAMETER['Central_Merid
ian',87.0],PARAMETER['Scale_Factor',0.9996],PARAMETER['Latitude_Of_Origin',0.0],U
NIT['Meter',1.0]]", "NO_PRESERVE_SHAPE", "")

# Process: Multiple Ring Buffer
arcpy.MultipleRingBuffer_analysis(Roads_Project, Roads_Buffer, "1;2;3;10", "Kilometers",
"distance", "ALL", "FULL")

# Process: Polygon to Raster (2)
arcpy.PolygonToRaster_conversion(Roads_Buffer, "distance", Roads__2_,
"CELL_CENTER", "distance", "30")

# Process: Reclassify (15)
```

```python
arcpy.gp.Reclassify_sa(Roads__2_, "Value", "1 10;1 2 8;2 3 3;3 10 3",
Reclass_Road_buffered, "DATA")

# Process: Line Density (2)
arcpy.gp.LineDensity_sa(Roads_Project, "NONE", Road_Density, "30",
"2621.95566120287", "SQUARE_KILOMETERS")

# Process: Reclassify (2)
arcpy.gp.Reclassify_sa(Road_Density, "Value", "0 0.84950944489123814
1;0.84950944489123814 2.4211019179400277 3;2.4211019179400277
5.0545811971028654 6;5.0545811971028654 10.831245422363281 9", Reclass_Road,
"DATA")

# Process: Clip (9)
arcpy.Clip_management(Precip_tif, "267740.263632764 2959088.21712711
353129.200928319 3067524.65976399", Precip_clip, AOI, "-2147483647",
"ClippingGeometry", "NO_MAINTAIN_EXTENT")

# Process: Project Raster
arcpy.ProjectRaster_management(Precip_clip, Precip_Project,
"PROJCS['WGS_1984_UTM_Zone_45N',GEOGCS['GCS_WGS_1984',DATUM['D_WGS_
1984',SPHEROID['WGS_1984',6378137.0,298.257223563]],PRIMEM['Greenwich',0.0],UN
IT['Degree',0.0174532925199433]],PROJECTION['Transverse_Mercator'],PARAMETER['F
alse_Easting',500000.0],PARAMETER['False_Northing',0.0],PARAMETER['Central_Merid
ian',87.0],PARAMETER['Scale_Factor',0.9996],PARAMETER['Latitude_Of_Origin',0.0],U
NIT['Meter',1.0]]", "NEAREST", Precip_clip, "", "", "")

# Process: Resample
arcpy.Resample_management(Precip_Project, Precip_Resample, "30 30", "NEAREST")

# Process: Reclassify (10)
arcpy.gp.Reclassify_sa(Precip_Resample, "Value", "1555 1770 6;1770 1915 7;1915 2100
8;2100 2250 9;2250 2560 10", Reclass_Precipitation, "DATA")

# Process: Clip (8)
arcpy.Clip_management(NDVI, "267740.263632764 2959088.21712711 353129.200928319
3067524.65976399", NDVI_Clip, AOI, "0.000000e+000", "ClippingGeometry",
"NO_MAINTAIN_EXTENT")

# Process: Reclassify (7)
arcpy.Reclassify_3d(NDVI_Clip, "Value", "-0.054468069225549698 0.25 1;0.25
0.68999999999999995 8;0.68999999999999995 0.998679101467132577 5", Reclass_NDVI,
"DATA")

# Process: Clip (7)
```

arcpy.Clip_management(DEM_tif, "267740.263632764 2959088.21712711 353129.200928319 3067524.65976399", DEM_Clip, AOI, "32767", "ClippingGeometry", "NO_MAINTAIN_EXTENT")

# Process: Project Raster (2)
arcpy.ProjectRaster_management(DEM_Clip, DEM_Project, "PROJCS['WGS_1984_UTM_Zone_45N',GEOGCS['GCS_WGS_1984',DATUM['D_WGS_1984',SPHEROID['WGS_1984',6378137.0,298.257223563]],PRIMEM['Greenwich',0.0],UNIT['Degree',0.0174532925199433]],PROJECTION['Transverse_Mercator'],PARAMETER['False_Easting',500000.0],PARAMETER['False_Northing',0.0],PARAMETER['Central_Meridian',87.0],PARAMETER['Scale_Factor',0.9996],PARAMETER['Latitude_Of_Origin',0.0],UNIT['Meter',1.0]]", "NEAREST", DEM_Clip, "", "", "")

# Process: Resample (3)
arcpy.Resample_management(DEM_Project, DEM_Resample, "30 30", "NEAREST")

# Process: Reclassify (9)
arcpy.gp.Reclassify_sa(DEM_Resample, "Value", "55 213 1;213 416 1;416 638 5;638 918 6;918 1241 7;1241 1590 8;1590 1800 9;1800 2584 10", Reclass_DEM, "DATA")

# Process: Aspect
arcpy.gp.Aspect_sa(DEM_Project, Aspect__2_)

# Process: Resample (2)
arcpy.Resample_management(Aspect__2_, Aspect_Resample, "30 30", "NEAREST")

# Process: Reclassify (13)
arcpy.gp.Reclassify_sa(Aspect_Resample, "Value", "-1 39.090901692708336 1;39.090901692708336 79.181803385416671 1;79.181803385416671 119.272705078125 2;119.272705078125 159.36360677083334 8;159.36360677083334 199.45450846354169 10;199.45450846354169 239.54541015625003 10;239.54541015625003 279.63631184895837 8;279.63631184895837 319.72721354166669 2;319.72721354166669 359.818115234375 1", Reclass_Aspect, "DATA")

# Process: Slope
arcpy.gp.Slope_sa(DEM_Project, Slope__2_, "DEGREE", "1")

# Process: Resample (4)
arcpy.Resample_management(Slope__2_, Slope_Resample, "30 30", "NEAREST")

# Process: Reclassify (12)
arcpy.gp.Reclassify_sa(Slope_Resample, "Value", "0 10 4;10 20 8;20 30 9;30 40 10;40 50 10;50 69.080848693847656 9", Reclass_Slope, "DATA")

# Process: Clip
arcpy.Clip_analysis(Thrusts___Faults, AOI, Thrusts_Clip, "")

Process: Project
```
arcpy.Project_management(Thrusts_Clip, Thrusts_Project,
"PROJCS['WGS_1984_UTM_Zone_45N',GEOGCS['GCS_WGS_1984',DATUM['D_WGS_
1984',SPHEROID['WGS_1984',6378137.0,298.257223563]],PRIMEM['Greenwich',0.0],UN
IT['Degree',0.0174532925199433]],PROJECTION['Transverse_Mercator'],PARAMETER['F
alse_Easting',500000.0],PARAMETER['False_Northing',0.0],PARAMETER['Central_Merid
ian',87.0],PARAMETER['Scale_Factor',0.9996],PARAMETER['Latitude_Of_Origin',0.0],U
NIT['Meter',1.0]]", "",
"GEOGCS['GCS_WGS_1984',DATUM['D_WGS_1984',SPHEROID['WGS_1984',6378137.
0,298.257223563]],PRIMEM['Greenwich',0.0],UNIT['Degree',0.0174532925199433]]",
"NO_PRESERVE_SHAPE", "")
```

Process: Multiple Ring Buffer (2)
```
arcpy.MultipleRingBuffer_analysis(Thrusts_Project, Thrusts_buffer, "2;4;6;8", "Kilometers",
"distance", "ALL", "FULL")
```

Process: Polygon to Raster (7)
```
arcpy.PolygonToRaster_conversion(Thrusts_buffer, "distance", Thrusts__2_,
"CELL_CENTER", "distance", "30")
```

Process: Reclassify (5)
```
arcpy.gp.Reclassify_sa(Thrusts__2_, "Value", "2 10;2 4 9;4 6 8;6 8 7;NODATA 1",
Reclass_Thrusts, "DATA")
```

Process: Clip (3)
```
arcpy.Clip_analysis(Settlement, AOI, Settlement_Clip, "")
```

Process: Project (3)
```
arcpy.Project_management(Settlement_Clip, Settlement_Project,
"PROJCS['WGS_1984_UTM_Zone_45N',GEOGCS['GCS_WGS_1984',DATUM['D_WGS_
1984',SPHEROID['WGS_1984',6378137.0,298.257223563]],PRIMEM['Greenwich',0.0],UN
IT['Degree',0.0174532925199433]],PROJECTION['Transverse_Mercator'],PARAMETER['F
alse_Easting',500000.0],PARAMETER['False_Northing',0.0],PARAMETER['Central_Merid
ian',87.0],PARAMETER['Scale_Factor',0.9996],PARAMETER['Latitude_Of_Origin',0.0],U
NIT['Meter',1.0]]", "",
"GEOGCS['GCS_WGS_1984',DATUM['D_WGS_1984',SPHEROID['WGS_1984',6378137.
0,298.257223563]],PRIMEM['Greenwich',0.0],UNIT['Degree',0.0174532925199433]]",
"NO_PRESERVE_SHAPE", "")
```

Process: Multiple Ring Buffer (3)
```
arcpy.MultipleRingBuffer_analysis(Settlement_Project, Settlement_buffer, "500;1000;2000",
"Meters", "distance", "ALL", "FULL")
```

Process: Polygon to Raster (4)

```
arcpy.PolygonToRaster_conversion(Settlement_buffer, "distance", Settlement__2_,
"CELL_CENTER", "NONE", "30")

# Process: Reclassify (4)
arcpy.Reclassify_3d(Settlement__2_, "Value", "500 10;500 1000 8;1000 2000 3;NODATA
0", Reclass_Settlement, "NODATA")

# Process: Clip (10)
arcpy.Clip_analysis(WATER_poly, AOI, WaterPoly_Clip, "")

# Process: Project (7)
arcpy.Project_management(WaterPoly_Clip, WaterPoly_Project,
"PROJCS['WGS_1984_UTM_Zone_45N',GEOGCS['GCS_WGS_1984',DATUM['D_WGS_
1984',SPHEROID['WGS_1984',6378137.0,298.257223563]],PRIMEM['Greenwich',0.0],UN
IT['Degree',0.0174532925199433]],PROJECTION['Transverse_Mercator'],PARAMETER['F
alse_Easting',500000.0],PARAMETER['False_Northing',0.0],PARAMETER['Central_Merid
ian',87.0],PARAMETER['Scale_Factor',0.9996],PARAMETER['Latitude_Of_Origin',0.0],U
NIT['Meter',1.0]]", "",
"GEOGCS['GCS_WGS_1984',DATUM['D_WGS_1984',SPHEROID['WGS_1984',6378137.
0,298.257223563]],PRIMEM['Greenwich',0.0],UNIT['Degree',0.0174532925199433]]",
"NO_PRESERVE_SHAPE", "")

# Process: Multiple Ring Buffer (5)
arcpy.MultipleRingBuffer_analysis(WaterPoly_Project, WaterPoly_Buffer, "1;2;3",
"Kilometers", "distance", "ALL", "FULL")

# Process: Polygon to Raster (5)
arcpy.PolygonToRaster_conversion(WaterPoly_Buffer, "distance", Water,
"CELL_CENTER", "distance", "30")

# Process: Reclassify (16)
arcpy.gp.Reclassify_sa(Water, "Value", "1 10;2 8;3 3;NODATA 1", Reclass_Water,
"DATA")

# Process: Clip (4)
arcpy.Clip_analysis(LANDSLIDES, AOI, Landslides_clip, "")

# Process: Multiple Ring Buffer (6)
arcpy.MultipleRingBuffer_analysis(Landslides_clip, Landslides_buffer, "500;1000;2000",
"Meters", "distance", "ALL", "FULL")

# Process: Polygon to Raster
arcpy.PolygonToRaster_conversion(Landslides_buffer, "distance", Landslides__2_,
"CELL_CENTER", "distance", "30")

# Process: Reclassify (3)
```

arcpy.Reclassify_3d(Landslides__2_, "Value", "500 10;500 1000 8;1000 2000 3;NODATA 0", Reclass_Landslides, "DATA")

# Process: Multiple Ring Buffer (4)
arcpy.MultipleRingBuffer_analysis(LINEAMENTS, Lineaments_buffer, "500;1000;2000", "Meters", "distance", "ALL", "FULL")

# Process: Polygon to Raster (8)
arcpy.PolygonToRaster_conversion(Lineaments_buffer, "distance", Lineaments__2_, "CELL_CENTER", "distance", "30")

# Process: Reclassify (6)
arcpy.Reclassify_3d(Lineaments__2_, "Value", "500 10;500 1000 8;1000 2000 3;NODATA 1", Reclass_Lineaments, "DATA")

Process: Weighted Sum
arcpy.gp.WeightedSum_sa("G:\\THESIS\\RISK_MAP\\inputs\\Landslide_risk.gdb\\Reclass_ Geology Value
7;G:\\THESIS\\RISK_MAP\\inputs\\Landslide_risk.gdb\\Reclass_Classification Value
6;G:\\THESIS\\RISK_MAP\\inputs\\Landslide_risk.gdb\\Reclass_Water_density Value
5;G:\\THESIS\\RISK_MAP\\inputs\\Landslide_risk.gdb\\Reclass_Lithology Value
5;G:\\THESIS\\RISK_MAP\\inputs\\Landslide_risk.gdb\\Reclass_Road_buffered Value
4;G:\\THESIS\\RISK_MAP\\inputs\\Landslide_risk.gdb\\Reclass_Road Value
3;G:\\THESIS\\RISK_MAP\\inputs\\Landslide_risk.gdb\\Reclass_Precipitation Value
2;G:\\THESIS\\RISK_MAP\\inputs\\Landslide_risk.gdb\\Reclass_NDVI Value
6;G:\\THESIS\\RISK_MAP\\inputs\\Landslide_risk.gdb\\Reclass_DEM Value
8;G:\\THESIS\\RISK_MAP\\inputs\\Landslide_risk.gdb\\Reclass_Aspect Value
5;G:\\THESIS\\RISK_MAP\\inputs\\Landslide_risk.gdb\\Reclass_Slope Value
9;G:\\THESIS\\RISK_MAP\\inputs\\Landslide_risk.gdb\\Reclass_Thrusts Value
10;G:\\THESIS\\RISK_MAP\\inputs\\Landslide_risk.gdb\\Reclass_Settlement Value
1;G:\\THESIS\\RISK_MAP\\inputs\\Landslide_risk.gdb\\Reclass_Water Value
4;G:\\THESIS\\RISK_MAP\\inputs\\Landslide_risk.gdb\\Reclass_Landslides Value
11;G:\\THESIS\\RISK_MAP\\inputs\\Landslide_risk.gdb\\Reclass_Lineaments Value 9", Landslide_risk)

# Process: Clip (11)
arcpy.Clip_management(Landslide_risk, "269148.591699998 3002768.867 352446.130999999 3066804.1465", Landslide_risk_clip, Terai_clipper_shp, "-3.402823e+038", "ClippingGeometry", "NO_MAINTAIN_EXTENT")

# Process: Reclassify (17)
arcpy.gp.Reclassify_sa(Landslide_risk_clip, "Value", "181 433 1;433 544 2;544 646 3;646 741 4;741 910 5", Reclass_landslide_risk_clip, "DATA")

Process: Raster to Polygon

```
arcpy.RasterToPolygon_conversion(Reclass_landslide_risk_clip, landslide_raster2poly,
"SIMPLIFY", "Value")

# Process: Dissolve
arcpy.Dissolve_management(landslide_raster2poly, landslide_risk_shp, "gridcode", "",
"MULTI_PART", "DISSOLVE_LINES")
```

BIOGRAPHICAL SKETCH

Terri Bannister is from southern Ontario, Canada. She attended the University of Waterloo for her undergraduate degree in Environmental Studies, with a concentration in Geomatics. She attended the University of Louisiana at Lafayette for her graduate degree in Science, specifically Geology.